Contributions to Mineralogy and Petrology (2020) 175:94
https://doi.org/10.1007/s00410-020-01731-y

ORIGINAL PAPER

# The intrinsic nature of antigorite breakdown at 3 GPa: Experimental constraints on redox conditions of serpentinite dehydration in subduction zones

**Juliette Maurice[1] · Nathalie Bolfan-Casanova[1] · Sylvie Demouchy[2] · Paul Chauvigne[1] · Federica Schiavi[1] · Baptiste Debret[3]**

Received: 3 May 2019 / Accepted: 12 August 2020 / Published online: 17 September 2020


## Abstract

Antigorite is considered as the most important source of water in subduction zones, playing a key role during arc magma genesis. Although, these magmas seem more oxidized than mid-oceanic ridge basalts (MORB), the possible inherent link between the oxidation state of arc magmas and serpentinite-derived hydrous fluids is still not well established. Here, we have performed dehydration experiments of natural antigorite serpentinite containing 5 weight percent (wt%) magnetite at 3 GPa and in a temperature range from 600 to 900 °C using a multi-anvil apparatus. These experiments aim to reproduce the different stages of $H_2O$ release, forming chlorite, olivine and orthopyroxene and water. Our experimental set up permits to preserve the intrinsic high oxygen fugacity ($fO_2$) of serpentinite during dehydration. The new olivine and orthopyroxene which formed in equilibrium with antigorite, chlorite and magnetite have high $X_{Mg}$ numbers setting up the oxygen fugacity to high values, between 3.1 and 4.1 log units above QFM (Quartz–Fayalite–Magnetite buffer). Hematite is observed concomitantly with high $X_{Mg}$ in olivine, of 0.94–0.97, generally at low temperatures, below 800 °C, in coexistence with chlorite. Once the magnetite is destabilized, upon chlorite breakdown which occurs above 800 °C, the oxygen fugacity decreases to 3.7 due to the decrease of the $X_{Mg}$ of silicates. This study demonstrates the highly oxidizing nature of the fluids released from antigorite dehydration. Thus, at high pressure and high temperature conditions, $f_{O2}$-sensitive elements such as carbon and sulfur are expected to be mobilized under their oxidized form, providing an oxidizing context for arc magmas genesis and assuming that they are not completely reduced by their percolation through meta-gabbro, meta-basalts and meta-sediments.

**Keywords** Antigorite · Serpentinites · Peridotite · Subduction · High-pressure research · Oxygen fugacity

## Introduction

Subduction of oceanic lithosphere is associated with material recycling in the mantle. In particular, the release of volatiles, such as $H_2O$, induces partial melting of the mantle wedge and is at the origin of arc magmatism (e.g. Ulmer and Trommsdorff 1995; Schmidt and Poli 1998; Gaetani and Grove 1998; Grove et al. 2006; Plank and Langmuir 1998). While hydrous lithologies among pelagic sediments and meta-basalts mostly dehydrate at relatively shallow depth in the fore-arc region (approximately 100 km of depth, e.g., Tatsumi 1989), ultramafic hydrated lithologies, such as serpentinites, can release large amounts of water at greater depths (150–200 km, Ulmer and Trommsdorff 1995). Serpentinites are rocks formed by the hydrothermal alteration and oxidation of Mg-rich silicates composing peridotites; they are mostly composed of serpentine, which is a layered

Communicated by Othmar Müntener.

**Electronic supplementary material** The online version of this article (https://doi.org/10.1007/s00410-020-01731-y) contains supplementary material, which is available to authorized users.

✉ Nathalie Bolfan-Casanova
nathalie.bolfan@uca.fr

[1] Université Clermont-Auvergne, CNRS, IRD, OPGC, Laboratoire Magmas Et Volcans, Campus des Cézeaux, 6 Avenue Blaise Pascal, 63178 Aubière, France

[2] Géosciences Montpellier, CNRS and Université Montpellier, Place E. Bataillon, 34095 Montpellier, France

[3] Laboratoire G-Time, DGES, Université Libre de Bruxelles, ULB, CP, 160/02, 1050 Brussels, Belgium

and hydrous phyllosilicate, plus a few percent of magnetite. Serpentinization of ultramafic rocks occurs in different geological settings: for example: on the oceanic seafloor of slow and ultra-slow spreading ridges (e.g., Cannat et al. 1990; Mevel 2003), at slab bending related faults (Ranero et al. 2003) and at the mantle wedge–slab interface when slab-related fluids are released (Deschamps et al. 2010; Guillot et al. 2000), rendering serpentinites ubiquitous in subduction zones (see Reynard et al. 2013; Guillot et al. 2015). Antigorite, the high temperature and high pressure serpentine variety (Evans et al. 1976; Mellini et al. 1987; Schwartz et al. 2013), is considered as the most important water carrier within the down-going lithospheric plate, as it is the most abundant hydrous silicate in ultramafic lithologies and the most hydrous with up to 12 wt.% $H_2O$. Therefore, antigorite breakdown which occurs upon slab subduction and thermal relaxation is the primary source of subduction-related aqueous fluids (Ulmer and Trommsdorff 1995; Schmidt and Poli 1998, 2014).

In addition to water release from the slab and its transfer to the mantle wedge, the speciation of the primary fluids will be controlled by the redox state of the rock from which they originate. The redox budget of serpentinite in subduction zones can be estimated using the $Fe^{3+}/\Sigma Fe$ ratio of the bulk rock (e.g., Evans 2006, 2012; Evans and Tomkins 2011; Evans and Powell 2015; Tumiati et al. 2015), as well as the content and speciation of C and S. What are the consequences of subducting a relatively oxidized serpentinized peridotite on the oxidation state of the fluids produced and the implications for the sub-arc mantle?

Samples of exhumed high-pressure serpentinites from ophiolites have allowed petrological characterization of antigorite dehydration reaction in natural settings**.** For instance, natural serpentinites from Cerro del Almirez (Debret et al. 2015; Garrido et al. 2005; López Sánchez-Vizcaíno et al. 2005; Padrón-Navarta et al. 2010a, b, 2011; Trommsdorff et al. 1998; Brestcher et al. 2018; Piccoli et al. 2019) and Cima di Gagnone (e.g., Evans and Trommsdorff 1978; Scambelluri et al. 2014; Piccoli et al. 2019) have helped constraining the reaction of antigorite destabilization into chlorite then olivine + enstatite nominally anhydrous assemblage. However, as discussed in the petrological models of Evans and Powell (2015) magnetite is the phase controlling the redox budget of serpentinite.

In addition to magnetite, occurrence of hematite in mafic and ultramafic lithologies from the Western Alps (e.g., Philippot and Selverstone 1991; Debret et al. 2016a) suggests that high $fO_2$, with values between QFM (Quartz–Fayalite–Magnetite buffer assemblage) + 2 and more than + 5, can be reached during antigorite breakdown (Debret and Sverjensky 2017), thus even above the hematite–magnetite buffer. Still, hematite had never been observed in experimental assemblages. This study aims to investigate the conditions of formation of hematite during antigorite dehydration.

Until recently, no experimental study was considering the fate of the iron oxide, namely magnetite, which accounts for ~ 5 wt.% of the bulk rock in most of serpentinites, at least in mid-ocean ridge settings (Andreani et al. 2013; Klein 2014). Merkulova et al. (2016, 2017) are the first to perform serpentine dehydration experiments focusing on the evolution of magnetite. Mixes of powdered natural antigorite and commercial magnetite were equilibrated at 1.5 to 2 GPa and different temperatures from 450 to 900 °C in a graphite furnace using the piston cylinder device. Their results point out to fluids being released at an oxygen fugacity of QFM-2, buffered by the graphite furnace. While Iacovino et al. (2020) monitored the oxygen fugacity during the dehydration of a natural serpentinite in the piston cylinder at 1 GPa and 800 °C using an $f_{O2}$ sliding sensor $Ni_xPd_{1-x}$. They measured a significantly higher oxygen fugacity of QFM + 2.

Thus, here, we examine the intrinsic oxygen fugacity of natural serpentinite after antigorite breakdown by performing high-pressure experiments in a multi-anvil press at 3 GPa and 600 to 900 °C. In a first series of experiments, we dehydrated a cylindrical sample of natural serpentinite containing 5 wt.% magnetite in contact with a layer of sintered San Carlos olivine, which acts as a fluid trap. In these experiments, hematite was produced. In following experiments, powdered samples were used, with or without olivine trap. The conditions imposed to the sample were also varied such as temperature, heating duration, capsule material or even furnace material. Initially, such experiments intended to let the sample evolve in a closed system as much as possible, using a passive environment with respect to the redox state of the starting material. The aim was to understand the key parameter controlling the formation of hematite during serpentinite dehydration experiments.

## Materials and methods

### Natural antigorite sample

Experiments were conducted using a natural serpentinite from the Iron Mountain, North Cascades, Washington, USA. The serpentinite is composed of a matrix of pure antigorite and oxides from the spinel group Fig. 1. No olivine, calcium-rich phases (diopside or tremolite) nor nickel-alloys have been observed in the investigated starting sample. To avoid $H_2O$ and $CO_2$ absorption expected to occur when grinded material is used, our starting sample was first prepared by drilling a cylinder from the rock specimen. Subsequently, to test whether equilibrium was attained in the experiments using cylinders, we also used powdered serpentinite. A sample from the same locality was investigated by Evans

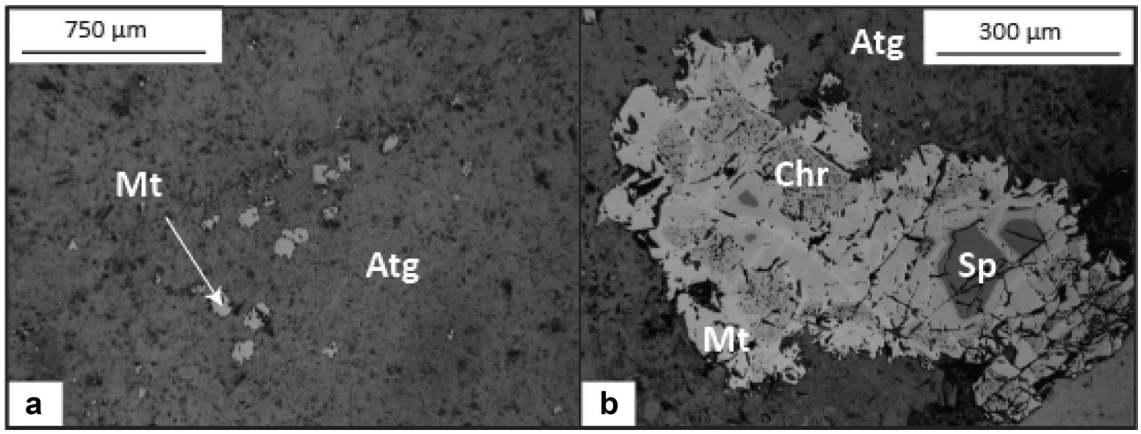


**Fig. 1** Microphotograph in reflective light of the serpentinite starting material from the Iron Mountain, North Cascades (Washington, USA), with **a** magnetite grains within the fine and dense antigorite matrix, and **b** composite oxides composed of Al-Cr spinel core surrounded by Al-poor, Fe-rich chromite and magnetite rims at the border

(2012, sample #IM3) using Mössbauer spectroscopy, yielding a $Fe^{3+}/\sum Fe$ ratio of 0.23 for the antigorite. The same value is assumed in this study. The composition of antigorite $Mg_{2.62}Fe^{2+}_{0.08}Fe^{3+}_{0.02}Al_{0.09}Cr_{0.01}Si_{1.97}O_{6.82}(OH)_{3.65}$ was obtained by means of an electron probe micro-analyzer and a $Fe^{3+}/\sum Fe$ ratio of 0.23. The calculated water content (12.05 wt.% $H_2O$) by stoichiometry) was obtained for an anticipated polysome (m = 17, Capitani and Mellini 2004) in agreement with the totals of electron probe analysis ranging around 86.5 ± 0.5%, see (Table 1, see also Maurice et al. 2018). Bulk analyses were performed using inductively coupled plasma atomic emission spectroscopy (ICP-AES) on 5 distinct batches of about 100 mg of serpentinite powder, separately grinded, to test the homogeneous distribution of magnetite grains within the bulk rock. The average of measurements of the bulk rock composition ($BR_1$) is reported in Table 1, as well as the standard deviation calculated from the 5 analyses. The only marginally higher amount of chromium in $BR_1$ (0.27 wt% $Cr_2O_3$) compared to antigorite (0.22 wt% $Cr_2O_3$), indicates a very minor proportion of chromite and associated spinel (< < 1%). Therefore, here, the redox budget of the bulk rock is determined by the modal amount of magnetite (Fig. 1a). Mass balance calculation based on the total iron content in the bulk rock (7.79 ± 0.48 wt.% $FeO_{total}$), in magnetite (91.32 wt.% $FeO_{total}$) and in antigorite (2.6 wt.% $FeO_{total}$ with a $Fe^{3+}/\sum Fe$ ratio = 0.23) indicates that the sample contains up to 5.5% magnetite in average, in agreement with analyses of backscattered images (as shown in Fig. 1a). It follows a calculated bulk rock composition, $BR_2$, made of 5.5 wt.% magnetite and 94.5 wt.% antigorite yielding a ratio of $Fe^{3+}/\sum Fe = 0.52$ (Table 1). The water content of the bulk rock was estimated by loss on ignition and equals to 11.40 wt.% $H_2O$, which agrees with an antigorite content in the bulk rock of 94.5%. The sulfur content has been measured using the Flash 2000 CHNS-O elemental analyzer from Thermo Fisher Scientific equipped with a 'MAS 200R' autosampler and reaches 150 ppm wt of S. The composition of the serpentinite used here is similar to the one from Cerro del Almirez (Padrón-Navarta et al. 2010a, b, 2011) or from the Voltri Massif in the Alps (Iacovino et al. 2020), both are reported in Table 1 for comparison. The composition is also similar to the average of serpentinites reported worldwide (see Iacovino et al. 2020, their Fig. 2).

The matrix of antigorite is dense, with rare porosity displayed in Fig. 1, due to thin section preparation. Two different occurrences of spinel group minerals have been observed: small grains of pure magnetite (100 µm in length) and oxide overgrowths displaying Cr-spinel-rich cores surrounded by chromite-rich and mantled by magnetite (Fig. 1b). These oxides occur as large aggregates, up to 900 µm in length. This type of oxides clusters is typical of serpentinites (e.g., Gervilla et al. 2012; Debret et al. 2014, their Fig. 3). Magnetite displays a composition close to the end-member. Despite intensive search, no pre-existing hematite was observed in the starting antigorite.

As already mentioned above, three types of starting material were used in this study (see Table 2). In the first experiments, an intact serpentinite cylinder was used together with a sintered polycrystalline olivine, acting as a fluid trap. The initial objective of the trap was to look at the interaction of a serpentinite and released fluid with an overlying wedge mantle, modeled here as dunite. However, this objective is beyond the scope of this paper and we focus here on the characterization of the oxygen fugacity experienced by the serpentinite during dehydration. In the second series of experiments we used powder of serpentinite together with a powder olivine trap. In the third series of experiments, we used only serpentinite powder without olivine trap. In this last series, we also varied the capsule material (AuPd or Au) and tested the presence/absence of magnetite in the

**Table 1** Average bulk rock (BR) chemical composition from ICP-AES (BR1) and standard deviation (from 5 distinct batches)

| | Serpentinite starting material | | | | | Previous studies | | | |
|---|---|---|---|---|---|---|---|---|---|
| | $BR_1$ | | $BR_2$ | Antigorite | | Almirez (a) | Mont-Cenis Alps (b) | Voltri Alps (c) | Model (d) |
| | ICP-AES | | Calc. | WDS | | | | | |
| $SiO_2$ | 40.04 | (0.30) | 40.79 | 43.17 | (0.51) | 40.34 | 38.02 | 41.54 | 37.1 |
| $TiO_2$ | 0.03 | (0.01) | 0.04 | 0.03 | (0.03) | 0.1 | 0.45 | 0.02 | – |
| $Al_2O_3$ | 1.63 | (0.11) | 1.57 | 1.66 | (0.36) | 2.81 | 1.92 | 1.44 | 1.89 |
| $Cr_2O_3$ | 0.27 | (0.00) | 0.28 | 0.22 | (0.08) | – | 0.16 | – | 0.51 |
| $FeO_{Total}$ | 7.79 | (0.48) | 7.48 | 2.60 | (0.17) | 6.7 | 6.07 | 7.44 | 11.9 |
| FeO | 3.52 | – | 3.57 | 2.00 | (0.13) | 2.87 | 1.9 | 4.61 | – |
| $Fe_2O_3$ | 4.65 | – | 4.35 | 0.66[e] | (0.04) | 4.26 | 4.8 | 2.54 | – |
| NiO | 0.25 | (0.00) | 0.15 | 0.16 | (0.03) | – | 0.04 | – | – |
| MnO | 0.09 | (0.00) | 0.07 | 0.07 | (0.04) | 0.09 | – | 0.11 | – |
| MgO | 38.94 | (0.40) | 36.45 | 38.56 | (0.41) | 37.48 | 38.52 | 37.43 | 35.5 |
| CaO | 0.02 | (0.02) | 0.02 | 0.02 | (0.02) | 0.07 | 2.43 | <0,01 | 0.01 |
| Total | 88.64 | (0.39) | 87.28 | 86.55 | (0.59) | 99.5 | 99.11 | 99.56 | 98.5 |
| $H_2O$ | 11.4[f] | | 11.39 [g] | 12.05 [h] | | 11.47 | 11.5 | 11.5 | 11.5 |
| $X_{Mg}$ | 0.90 | | 0.90 | 0.96 | | 0.91 | | 0.90 | 0.84 |
| Redox budget [i] | 0.25 | | | | | 0.23 | 0.25 | 0.14 | |

Bulk rock composition calculated for 94.5% antigorite and 5.5% magnetite is reported as BR2

[a]Padrón-Navarta et al. (2011)

[b]Merkulova et al. (2016)

[c]Iacovino et al. (2020)

[d]Piccoli et al. (2019)

[e]$Fe_2O_3$ estimated from $\sum Fe^{3+}/Fe_{total}$ of 0.23 (similar to sample IM3, Evans et al. 2012)

[f]$H_2O$ content calculated from loss on ignition

[g]$H_2O$ content estimated from modal amount of antigorite in BR

[h]$H_2O$ content from structural formula

[i]The redox budget is calculated as $1/2 \times Fe_2O_3$ content in moles per mole, see Evans and Powell (2015)

starting material (the initial rock was grinded and magnetite was separated with a magnet). In addition, to evaluate the effect of volatile species on the redox potential of the fluids expelled from antigorite dehydration, we also performed two additional experiments where we added Cl (in the form of NaCl, 1 wt%) and S (in the form of FeS, 1 wt.%), mixed with the serpentinite powder.

## High-pressure experiments

Breakdown of antigorite was performed using a multi-anvil press at 3 GPa and 600–900 °C with varying run durations. The multi-anvil apparatus was preferred over piston-cylinder because of furnace versatility. Experimental conditions are reported in Table 2. Experiments were conducted with 25 and 18 mm edge length octahedra made of MgO + 5% $Cr_2O_3$ and WC cubes of 32 mm edge with 17 and 11 mm truncation, respectively. The pressure in the 25 mm assembly was calibrated using three systems: (i) Bi I-II phase transition occurring at 2.5 GPa and room temperature (Bean et al. 1986), (ii) the coesite/stishovite phase transition of $SiO_2$ at 8.01 GPa at 800 °C (Zhang et al. 1996) and (iii) the garnet to perovskite phase transition of $CaGeO_3$ at 6.2 GPa and 1000 °C (Susaki et al. 1985). For experiments using the 18/11 assemblies see (Maurice et al. 2018). All the ceramic parts (except graphite) of the high-pressure cell were fired at 1000 °C for 30 min prior to loading the capsule and cementing.

The samples were placed in noble metal capsules, $Au_{80}Pd_{20}$ or Au (length: 4.3 mm, diameter: 3 mm, in the 25 M assembly; length: 2.7 mm, diameter: 2 mm for the 18 M assembly; wall thickness: 0.35 mm), which is then arc-welded at the top and bottom. The capsule was insulated from the furnace by an MgO sleeve. We also used the $Ni_xPd_{1-x}$ oxygen fugacity sensor following Matjuschkin et al. (2015). We mixed a 1:1 molar NiO and Pd powder with 3 µl of water which was inserted in an alumina tube tapped with alumina powder to be insulated from the Pt capsule (instead of AuPd or Au capsule to avoid contamination of the sensor by Au). This experiment was held at 800 °C and 3 GPa for

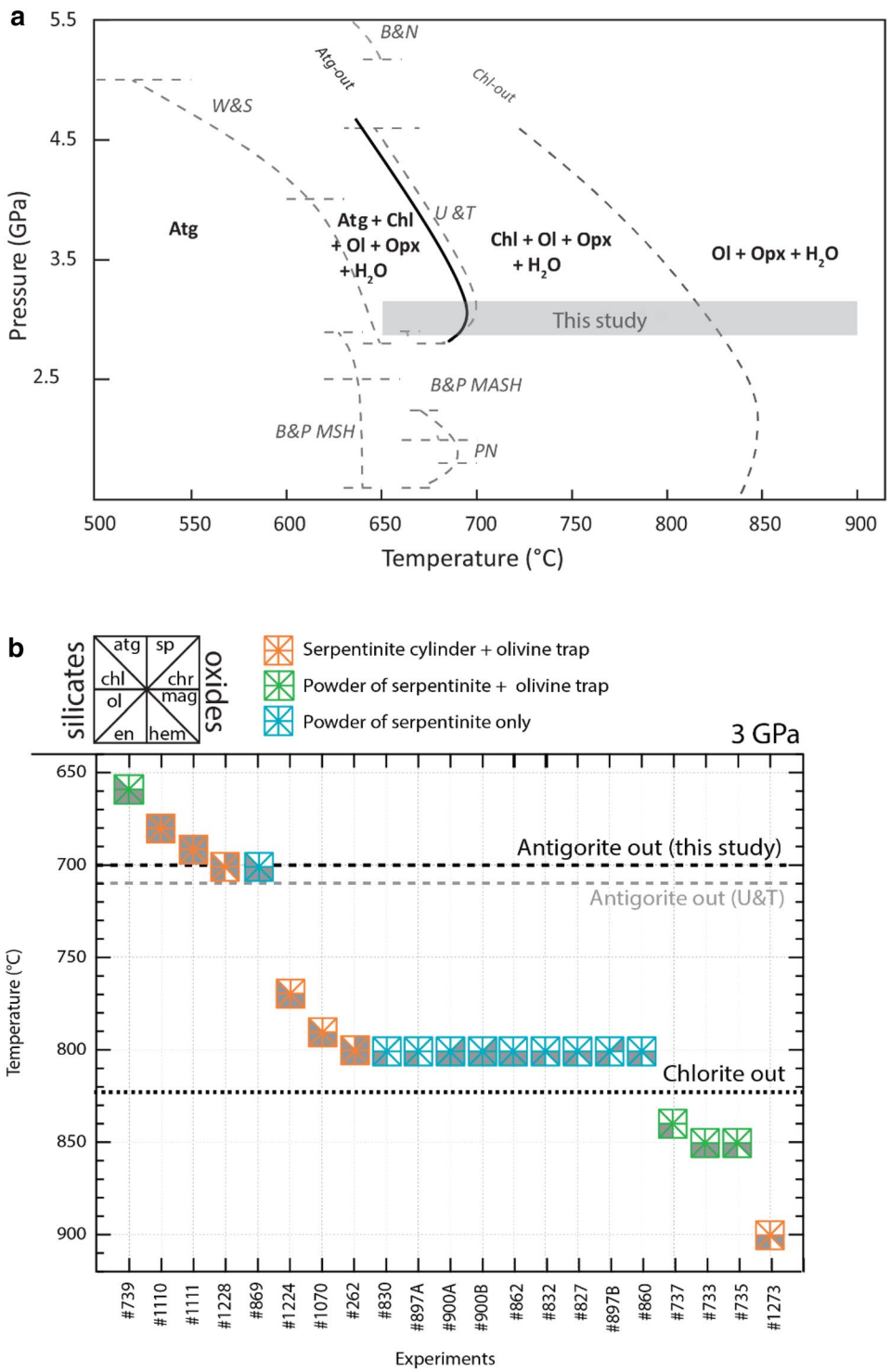


**Fig. 2** **a** Experimental pressure–temperature stability field of antigorite. The gray bar represents the field of investigation in this study. The antigorite-out curve from other experimental studies are shown as annotated dashed lines. Abbreviations are as follow; U&T: Ulmer and Trommsdorff (1995); W&S: Wunder and Schreyer (1997); B&N: Bose and Navrotsky (1998), PN: Padrón-Navarta et al. (2010a); B&P: Bromiley and Pawley (2003) for both MSH and MASH systems. **b** Mineral paragenesis for each experiment

5 h (#M865). The equilibration of the $Ni_xPd_{1-x}$ sensor yields $X_{Ni}$ in the alloy of 0.25 in mole fraction, equivalent to a $\log(f_{O2})$ of -11.3 bars.

The furnace was in most experiments made of $LaCrO_3$ and two experiments used C (graphite) to test whether the furnace alters the oxygen fugacity within the sample during the time of the experiment. The furnace shape was stepped to reduce thermal gradients along the capsule. Temperature was measured using a Pt/Rh thermocouple in contact with the capsule. The thermal gradient was simulated using the finite element method by Hernlund et al. (2006) and yields a thermal gradient less than 30 °C/mm when using $LaCrO_3$ furnace and less than 11 °C/mm when using graphite furnace. The final pressure was obtained following a steady

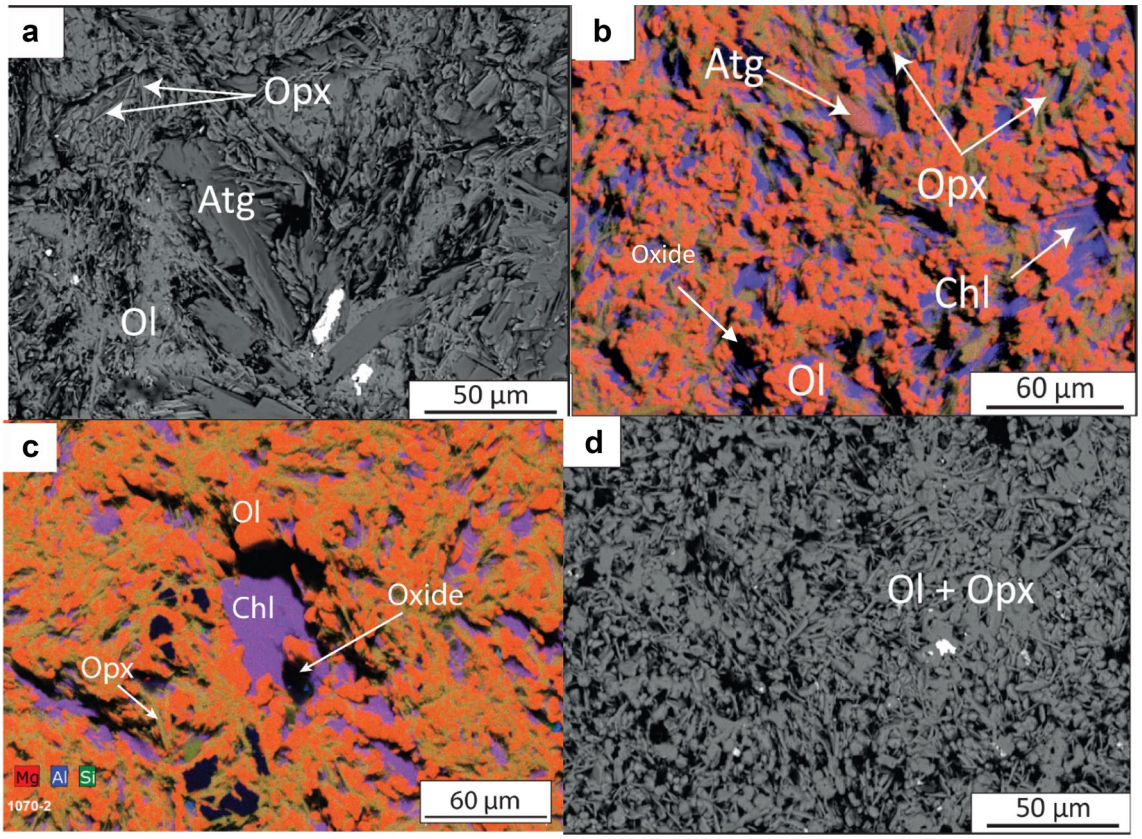


**Fig. 3** Scanning Electron Microscope images illustrating the characteristic microstructures of the samples after antigorite dehydration. **a** Backscatter electron scanning (BSE) image showing typical mineralogical assemblage and texture with secondary antigorite, olivine and orthopyroxene (#1110 synthesized at 680 °C). **b** Corresponding chemical map by Energy-dispersive X-ray spectroscopy, evidencing the presence of also chlorite and magnetite. Color-coding is as follows: olivine = red–orange, chlorite = purple, antigorite = brown, and orthopyroxene = pale green dendrites, oxide = black. **c** Chemical map of sample #1070 (synthesized at 790 °C) where chlorite coexists with olivine and orthopyroxene and an oxide. **d** BSE image of a sample after complete breakdown of the hydrous phases showing only olivine and orthopyroxene (#1273, 900 °C)

increase ramp within 2 h to reach 3 GPa and pressure was maintained constant for 3–24 h (Table 2). Turning off the power quenched the experiments and the pressure was automatically decreased over 8–9 h (i.e., slow decompression) to minimize cracks formation.

### Characterization of run products

After the experiments, the capsules were embedded in a dental resin and gently hand-polished with 1200 µm grid silicon carbide paper, then polished using 6, 3 and ¼ µm diamond paste and subsequently carbon coated prior to chemical analyses. First, chemical characterization was performed using a scanning electron microscopy (SEM) and Energy-dispersive X-ray spectroscopy (EDS) mapping. Then, electron probe microanalyses (EPMA) were performed to obtain the chemical composition of the products of antigorite dehydration. The beam current and intensity was set to 15 keV and 15 nA, respectively, for olivine and enstatite and the intensity was lowered to 8 nA for antigorite and other hydrous minerals. A point beam set up (1 µm in diameter) was used Table 3.

## Results

### Textural and chemical evolution of the dehydration products

Different silicates and oxides assemblages (all $H_2O$ saturated) were found as a result of increasing temperature. Run conditions and product phases are reported in Table 2 and in a pressure–temperature diagram in Fig. 2. The compositions in major elements in all co-existing silicate phases are reported in Table 3. Oxides major elements compositions are reported in Table 4. At 3 GPa, antigorite is stable at a temperature up to 690 °C, in agreement with the stability field of antigorite presented in previous studies (e.g., Bose and Navrotsky 1998; Bromiley and Pawley 2003;

**Table 2** Experimental run conditions and resulting mineral assemblages, pressure is 3 GPa

| | Duration (hrs) | T [(d)] (°C) | Silicate products | Oxides products | Capsule material | *X*Mg olivine | stdv | nbr grains | *X*Mg opx | stdv | nbr grains | $f_{O2}$ ΔQFM[(g)] |
|---|---|---|---|---|---|---|---|---|---|---|---|---|
| *Ist series: rod sepentinite and olivine trap* | | | | | | | | | | | | |
| #1110 | 12 | 680 | Atg2, Chl, Ol, En | Spinel + hem | AuPd | 0.95 | 0.05 | 4 | 0.953 | 0.05 | 4 | 3.5 |
| #1111 | 3 | 690 | Atg2, Chl, Ol, En | Spinel + hem | AuPd | 0.94 | 0.09 | 7 | 0.95 | 0.02 | 3 | 3.3 |
| #1228[c] | 10 | 700 | Chl, Ol, En | Spinel | AuPd | 0.94 | 0.13 | 8 | 0.95 | 0.05 | 4 | 3.6 |
| #1224 | 10 | 770 | Chl, Ol, En | Spinel + hem | AuPd | 0.95 | 0.12 | 8 | 0.95 | 0.03 | 4 | 3.5 |
| #1070 | 6 | 790 | Chl, Ol, En | Spinel + hem | AuPd | 0.96 | 0.06 | 10 | 0.94 | 0.06 | 3 | 3.9 |
| #262 | 5 | 800 | Chl, Ol, En | Spinel + hem | AuPd | 0.97 | 0.04 | 5 | 0.96 | 0.02 | 4 | 4.7 |
| #1273[c] | 5 | 900 | Ol, En | Soinel | AuPd | 0.94 | 0.07 | 6 | 0.93 | 0.12 | 7 | |
| 2nd series: powdered serpentinite and olivine trap | | | | | | | | | | | | |
| #739[a] | 5 | 660 | Chl, Ol, En | Spinel + hem | AuPd | 0.94 | 0.007 | 4 | 0.95 | 0.01 | 3 | 3.1 |
| #733 | 5 | 850 | Ol, En | Spinel + hem | AuPd | 0.95 | 0.005 | 6 | 0.94 | 0.94 | 2 | 3.7 |
| #735[b] | 5 | 850 | Ol, En | Spinel | AuPd | 0.89 | 0.006 | 7 | 0.93 | 0.01 | 3 | |
| #737 | 12 | 840 | Ol, En | Not observed | AuPd | 0.90 | 0.014 | 5 | 0.92 | 0.01 | 4 | |
| 3rd series:powdered serpentinite without olivine trap | | | | | | | | | | | | |
| Effect of the capsule | | | | | | | | | | | | |
| #830 | 12 | 800 | Ol, En | Not observed | AuPd[(f)] | 0.93 | 0.00 | 8 | 0.94 | 0.00 | 12 | |
| #897A | 12 | ≥800 | Ol, En | Not observed | Au[(f)] | 0.96 | 0.00 | 7 | 0.97 | 0.00 | 5 | |
| #900A | 12 | 800 | Ol, En | Spinel + hem | AuPd | 0.97 | 0.008 | 12 | 0.94 | 0.01 | 10 | 4.8[(e)] |
| #900B | 12 | 800 | Ol, En | Spinel + hem | Au | 0.96 | 0.006 | 10 | 0.92 | 0.01 | 8 | 4.1[(e)] |
| Effect of heating duration | | | | | | | | | | | | |
| #869 | 12 | 700 | Chl, Ol, En | Spinel + hem | AuPd | 0.97 | 0.007 | 6 | 0.95 | 0.01 | 4 | 4.5[(e)] |
| #862 | 12 | ≤800 | Ol, En | Spinel + hem | AuPd | 0.96 | 0.009 | 7 | 0.95 | 0.02 | 6 | 4.1 |
| #832 | 12 | ≥800 | Ol, En | Spinel | AuPd | 0.88 | 0.05 | 11 | 0.94 | 0.01 | 7 | |
| #827 | 24 | 800 | Ol, En | Spinel | AuPd | 0.90 | 0.03 | 14 | 0.94 | 0.01 | 4 | |
| #897B | 12 | ≥800 | Ol, En | Rare spinel | Au | 0.90 | 0.005 | 6 | 0.92 | 0.01 | 4 | |
| #860 | 24 | 800 | Ol, En | Spinel | Au | 0.92 | 0.006 | 20 | 0.93 | 0.00 | 5 | |

[a]1wt% NaCl added in the starting material

[b]1 wt% FeS added in the starting material

[c]Experiment performed using a graphite capsule

[d]Maximum thermal gradient is of 30 °C/mm

[e]The fO2 of these samples were not considered in Fig. 9 because the $Kd_{Fe\text{-}Mg}^{olivine/enstatite}$ is too low

[f]No magnetite in the starting material

[g]$\Delta QFM = \log f_{O2(sample)} - \log f_{O2(QFM)}$, with $\log f_{O2(QFM)} = 82.75 + 0.00484\ T - 30{,}681/T - 24.45 \log T + 940\ P/T - 0.02\ P$, with T in Kelvins and P in GPa (from O'Neill et al. 1987)

Padrón-Navarta et al. 2010a; Ulmer and Trommsdorff 1995; Wunder and Schreyer 1997). Each reaction stage is detailed below, first for the silicate components followed by the co-existing oxides.

## Silicates

After partial dehydration at 680 and 690 °C, antigorite coexists with chlorite, olivine, enstatite and water. The texture displays high porosity (10%) with tabular Atg (10–80 µm long) and xenomorphic chlorite + olivine + enstatite (10 µm size maximum, see Fig. 3a). Enstatite is characterized by needle-like crystals, either well defined or inter-grown with olivine (see Fig. 3a and c). Pyroxene crystals are often very small and thin, thus quite difficult to analyze. Chlorite is easily identified in EDS maps due to its high alumina content as illustrated in Fig. 3b and c, it crystallizes as interstitial small grains (5–10 µm width) co-existing with olivine and orthopyroxene.

At temperatures above or equal to 700 °C, antigorite is completely transformed into chlorite + olivine + enstatite + $H_2O$. The product assemblage consists in an aggregate of small rounded crystals of olivine (5–10 µm) inter-grown with acicular to needle-like enstatite prisms (up to 30 µm in length). The composition of chlorite is close to clinochlore $(Mg,Fe)_5Al(Si_3Al)O_{10}(OH)_8$. When chlorite coexists with antigorite, chlorite contains 12.4–12.9 wt. % $Al_2O_3$. Once antigorite breaks down, chlorite becomes enriched in aluminum with concentration up to 13–15.5 wt. % $Al_2O_3$ (see Fig. 4).

At temperatures at or above 800 °C, the hydrous phases have completely disappeared and only the nominally anhydrous olivine and enstatite remain ± the oxides (see Fig. 3d). No garnet is observed in the mineral assemblage and this absence is probably due to the refractory character of the protolith which has relatively a low alumina content (1.6 wt.% $Al_2O_3$) as well as the fact that most of the Al can be accommodated in the enstatite (with contents that vary from 1.7 ± 0.2 at 680 °C to 5.0 ± 0.8 wt% $Al_2O_3$ at 900 °C). The incorporation of Al in the pyroxene seems to follow a Tschermak's substitution ($Mg^{2+} + Si^{4+} = 2Al^{3+}$) as shown in Fig. 5).

The $X_{Mg}$ of olivine is on average 0.96 ± 0.01 at temperatures ≤ 850 °C (see Fig. 6), close to the $X_{Mg}$ of the starting antigorite (0.96, see Table 1) and of chlorite ($X_{Mg}$ ~ 0.95). In the two samples where magnetite was removed from the starting serpentinite powder (#830 and #897A), olivine displays high $X_{Mg}$ ranging from 0.93 to 0.96. With increasing temperature (i.e. above 800 °C) magnetite breaks down and olivine incorporates more iron and consequently its $X_{Mg}$ decreases down to 0.88–0.89 (#827, #832, #897B). In one sample which was heated at a higher temperature of 850 °C for 12 h, (#737), no magnetite is observed anymore and olivine composition is homogeneous with $X_{Mg}$ = 0.89, close to that of mantle olivine i.e. similar to the potential protolith before serpentinization (see BR in Table 1). Coexisting orthopyroxene usually have $X_{Mg}$ values ranging from 0.94 ± 0.2. In any case, the partitioning of iron between olivine and orthopyroxene follows the same trend, although with some scatter, maybe owing to the aluminum incorporation in orthopyroxene, as observed by von Seckendorf and O'Neill (1987) at higher temperatures, (see discussion and supplementary Fig. 1a).

## Oxides

The different oxides (chromite spinel, magnetite, hematite) are easily distinguished by their different optical properties in reflected light (see Supplementary Fig. 2). Their structure was confirmed by Raman spectroscopy (Fig. 7) and their chemical composition by electron microprobe (Table 4, and Fig. 8). Optically zoned chromite grains display the common Fe-rich rim with higher reflectance, i.e. the grains consist of a dark core surrounded by a rim that changes gradually in composition (enriched in Fe and depleted in Mg, Al and Cr) towards magnetite at the border. The cores are relatively homogeneous in composition and are inherited from the protolith (see Figs. 1 and 8; Bliss and MacLean 1975; Gervilla et al. 2012). The average compositions representing these three poles are $(Mg_{0.55}Fe_{0.5})(Al_{1.14}Cr_{0.8})O_4$ for the core, $(Mg_{0.08}Fe_{0.92})(Fe_{1.05}Al_{0.06}Cr_{0.8})O_4$ for the intermediate ferri-chromite to $(Mg_{0.1}Fe_{0.9})(Fe_2Al_{0.001}Cr_{0.04})O_4$ in the magnetite rim. This magnetite rim has been recognized to form during serpentinization or prograde metamorphism (Bliss and MacLean 1975; Burkhard 1993; Gervilla et al. 2012). The composition of magnetite varies from $(Fe_{0.72}Mg_{0.28})(Fe_{1.96}Cr_{0.03})O_4$ to $Fe_{2.94}Cr_{0.04}O_4$ (see Table 4).

## Presence/absence of hematite

In several experiments hematite is observed as lamellae crossing pre-existing magnetite grains as shown in Fig. 7 or supplementary Fig. 2. The composition of hematite varies from $Fe_{1.92}O_3$ to $Fe_{1.97}O_3$. Hematite is observed concomitantly with high $X_{Mg}$ in olivine, of 0.94–0.97 (see Fig. 6). These features usually occur at temperatures below 800–850 °C, often in coexistence with antigorite and/or chlorite. Hematite is not observed in experiments using graphite furnace at 700 and 900 °C. It is mostly observed in AuPd-capsules but also in one Au-capsule experiments (#900B, see Table 2). It is observed in presence or in absence of olivine trap.

### Oxygen fugacity prevailing during the experiments

The oxygen fugacity can be constrained using the silicate phase assemblage when either hematite or magnetite are stable. In experiments where hematite was observed, the oxygen fugacity, $f_{O2}$, can be calculated using the equilibrium between quartz, fayalite and hematite (QFH):

$$2Fe_2SiO_4 + O_2 = 2\,SiO_2 + 2\,Fe_2O_3 \quad (1)$$

It follows

$$\log f_{O2} = 2\log a_{SiO2} + 2\log a^{hematite}_{Fe2O3} - 2\log a^{olivine}_{Fe2SiO4} + \Delta G_1/(\ln(10).RT) \quad (2)$$

where R is the real gas constant and T is temperature in Kelvins. The activity of silica was calculated using the equilibrium between the magnesian end-members of olivine and pyroxene, following Stagno and Frost (2010):

$$Mg_2SiO_4 + SiO_2 = Mg_2Si_2O_6 \quad (3)$$

i.e.

$$\log a_{SiO2} = \log a^{orthopyroxene}_{Mg2Si2O6} - \log a^{olivine}_{Mg2SiO4} + \Delta G_3/(\ln(10).RT) \quad (4)$$

The Gibbs energies were calculated using the thermodynamic parameters of the end-members of the solid solutions (see Table 5) and using the activities, $a_i$, of the end-members in the phases $a_{SiO2}$, $a^{orthopyroxene}_{Mg2Si2O6}$, $a^{olivine}_{Mg2SiO4}$, $a^{olivine}_{Fe2SiO4}$, which were calculated from Table 3 using the expressions of the activity coefficients given in Table 5. The samples are compared throughout all this study to the QFM buffer that was also calculated at 3 GPa and 660–900 °C using the thermodynamic database in Table 5, to obtain internally consistent oxygen fugacity values. Our calculation of QFM agrees within 0.4 log units of the formulation of QFM provided by Ballhaus et al. (1991) and O'Neill et al. (1987) from 600 to 1000 °C.

The oxygen fugacities of the samples calculated using the above QFH equilibrium, range between 3.1 and 4.1 log units above QFM (see Table 2 and Fig. 9). The oxygen fugacity increases slightly with increasing temperature in the chlorite stability field and then decreases with decreasing $X_{Mg}$ of olivine. Once chlorite disappears between 800 and 850 °C, the oxygen fugacity continues to decrease from 4.1 to 3.7 log units above QFM.

### Attainment of equilibrium

We are able to confirm the attainment of local equilibrium in most experiments, as evidenced by the change in mineral compositions with experimental conditions, in particular the increase in Al content in orthopyroxene and chlorite with increasing temperature (see Fig. 4). However, if we use the exchange of iron between olivine and orthopyroxene, as defined in reaction (5) below, we can identify samples that depart from the trend established experimentally for mixes of olivine and enstatite at 900, 1000 and 1100 °C at 1.6 GPa (von Seckendorf and O'Neill, 1987, see Supplementary Fig. 1b):

$$Mg_2SiO_4 + Fe_2Si_2O_6 = Fe_2SiO_4 + Mg_2Si_2O_6 \quad (5)$$

The exchange partition coefficient of Fe between olivine and orthopyroxene can be defined as

$$Kd^{Ol/Opx}_{Fe-Mg} = \left(X^{Ol}_{Fe}.X^{Opx}_{Mg}\right)/\left(X^{Ol}_{Mg}.X^{Opx}_{Fe}\right) \quad (6)$$

Microprobe analysis of the run products indicate a $Kd_{Fe-Mg}^{Ol/Opx}$ varying between 0.5 and 1.9, while expected values should lie around 1. Note that for the samples where magnetite was removed from the starting material $Kd_{Fe-Mg}^{Ol/Opx}$ is of 1.1. Most samples of this study follow the partitioning of iron between olivine and orthopyroxene close to $1.0 \pm 0.2$ as shown in Supplementary Fig. 1b. However, there are some outliers that show very high values of 1.5–1.9 or very low values of 0.5–0.8. The high values of $Kd_{Fe-Mg}^{Ol/Opx}$ correspond to samples where destabilization of magnetite was readily observed, i.e. when magnetite was dissolving into silicates. While the low values of $Kd_{Fe-Mg}^{Ol/Opx}$ correspond to some samples that were co-existing with hematite (#900A, #900B, #869). Thus, for these three samples, the calculated oxygen fugacity is probably largely unconstrained, so they were removed from the discussion in Fig. 9. Even if we discard the experiments with anomalous $Kd_{Fe-Mg}^{Ol/Opx}$, and only keep the experiments which display $Kd_{Fe-Mg}^{Ol/Opx}$ of $1.0 \pm 0.2$, we find that the products of dehydration of natural antigorite display $\log(f_{O2})$ values between 3.1 and 4.1 relative to the QFM buffer.

## Discussion

### Antigorite stability field

The present starting antigorite is Fe- and Al-poor compared to the natural specimens from Cerro del Almirez previously studied by Debret et al. (2015) and Padrón-Navarta et al. (2008, 2011) (see Table 1) and from other experimental compositions. Thus, as expected, we found small variations of the stability field of antigorite. For example, Ulmer and Trommsdorff (1995) investigated the antigorite breakdown of a material composed of a mixture of 85 volume percent (vol %) of natural antigorite (1.30 wt. % $Al_2O_3$, 2.94 wt% FeO) and 15 vol % brucite, to which was added 10 wt% of

**Table 3** Chemical compositions of antigorite and dehydration products from EPMA. N= number of analysis

| Experiment | #1110 | | | | | | | | #1111 | | | | | | | | #1228 | | | | | | #1224 | | | | | | #1070 | | | | | |
|---|---|---|---|---|---|---|---|---|---|---|---|---|---|---|---|---|---|---|---|---|---|---|---|---|---|---|---|---|---|---|---|---|---|---|
| Mineral | Atg2 | | Chl | | Ol | | En | | Atg | | Chl | | Ol | | En | | Chl | | Ol | | En | | Chl | | Ol | | En | | Chl | | Ol | | En | |
| n | 8 | | 3 | | 4 | | 4 | | 10 | | 1 | | 7 | | 3 | | 2 | | 8 | | 4 | | 4 | | 8 | | 4 | | 4 | | 10 | | 3 | |
| SiO2 | 43.78 | (0.48) | 36.36 | (1.29) | 42.38 | (1.39) | 59.11 | (1.22) | 43.30 | (0.78) | 36.18 | | 42.34 | (1.03) | 57.40 | (1.00) | 36.95 | (1.49) | 41.60 | (1.06) | 58.01 | (1.01) | 34.01 | (0.63) | 42.11 | (0.94) | 57.46 | (1.04) | 34.80 | (0.89) | 42.50 | (1.23) | 56.80 | (0.85) |
| TiO2 | 0.03 | (0.04) | 0.33 | (0.47) | 0.01 | (0.01) | 0.01 | (0.01) | 0.03 | (0.04) | 0.05 | | 0.04 | (0.04) | 0.05 | (0.06) | 0.02 | (0.03) | 0.03 | (0.03) | 0.02 | (0.04) | 0.01 | (0.01) | 0.06 | (0.06) | 0.01 | (0.02) | 0.01 | (0.02) | 0.03 | (0.05) | 0.03 | (0.03) |
| Al2O3 | 1.06 | (0.35) | 12.43 | (0.37) | 0.11 | (0.07) | 1.67 | (0.23) | 1.47 | (0.76) | 12.86 | | 0.21 | (0.14) | 2.58 | (0.16) | 13.00 | (1.21) | 0.17 | (0.16) | 2.59 | (0.23) | 15.52 | (0.57) | 0.14 | (0.13) | 2.41 | (0.23) | 14.27 | (0.73) | 0.14 | (0.14) | 3.00 | (0.59) |
| Cr2O3 | 0.24 | (0.06) | 0.72 | (0.12) | 0.16 | (0.05) | 0.33 | (0.04) | 0.15 | (0.09) | 0.84 | | 0.15 | (0.11) | 0.24 | (0.09) | 1.10 | (0.17) | 0.20 | (0.06) | 0.24 | (0.06) | 0.83 | (0.16) | 0.23 | (0.06) | 0.20 | (0.06) | 0.82 | (0.09) | 0.23 | (0.13) | 0.30 | (0.10) |
| FeO | 2.71 | (0.15) | 2.62 | (0.40) | 4.78 | (0.46) | 3.22 | (0.33) | 3.06 | (0.29) | 2.83 | | 5.82 | (0.85) | 3.68 | (0.17) | 2.88 | (0.04) | 6.11 | (1.24) | 3.02 | (0.20) | 3.05 | (0.19) | 4.49 | (1.19) | 3.55 | (0.26) | 3.16 | (0.13) | 4.29 | (0.63) | 3.08 | (0.06) |
| NiO | 0.17 | (0.05) | 0.17 | (0.05) | 0.29 | (0.06) | 0.10 | (0.02) | 0.16 | (0.04) | 0.17 | | 0.25 | (0.05) | 0.11 | (0.07) | 0.16 | (0.00) | 0.23 | (0.03) | 0.13 | (0.03) | 0.16 | (0.04) | 0.24 | (0.06) | 0.11 | (0.04) | 0.16 | (0.11) | 0.20 | (0.12) | 0.11 | (0.06) |
| MnO | 0.09 | (0.03) | 0.03 | (0.03) | 0.15 | (0.03) | 0.09 | (0.04) | 0.06 | (0.04) | 0.00 | | 0.13 | (0.03) | 0.09 | (0.02) | 0.03 | (0.04) | 0.10 | (0.03) | 0.06 | (0.04) | 0.02 | (0.03) | 0.08 | (0.07) | 0.10 | (0.02) | 0.02 | (0.02) | 0.09 | (0.04) | 0.08 | (0.02) |
| MgO | 39.24 | (0.68) | 35.18 | (0.47) | 52.02 | (1.41) | 36.86 | (0.41) | 39.15 | (0.46) | 34.61 | | 51.41 | (0.79) | 36.79 | (0.74) | 33.83 | (0.41) | 50.87 | (1.15) | 36.28 | (0.95) | 34.56 | (0.27) | 52.63 | (1.11) | 36.02 | (0.47) | 34.63 | (0.51) | 52.35 | (0.79) | 37.20 | (2.50) |
| CaO | 0.01 | (0.02) | 0.15 | (0.09) | 0.00 | (0.00) | 0.01 | (0.01) | 0.01 | (0.02) | 0.00 | | 0.00 | (0.00) | 0.03 | (0.03) | 0.03 | (0.02) | 0.02 | (0.02) | 0.07 | (0.04) | 0.03 | (0.02) | 0.01 | (0.01) | 0.03 | (0.01) | 0.04 | (0.07) | 0.02 | (0.02) | 0.04 | (0.06) |
| Total | 87.33 | (1.01) | 88.00 | (0.00) | 99.91 | (0.55) | 101.40 | (1.12) | 87.40 | (0.81) | 87.55 | | 100.34 | (0.69) | 100.97 | (0.39) | 88.00 | (0.00) | 99.32 | (0.66) | 100.44 | (2.07) | 88.18 | (0.35) | 99.99 | (0.77) | 99.90 | (1.52) | 87.91 | (0.42) | 99.86 | (0.70) | 100.62 | (3.93) |
| Ions calculated on the basis of 6.824 equivalent oxygens (polysom m=17) for antigorite, 14 for chlorite, 4 for olivine and 6 for orthopyroxene | | | | | | | | | | | | | | | | | | | | | | | | | | | | | | | | | | |
| Si | 1.98 | (0.01) | 3.37 | (0.10) | 1.01 | (0.03) | 1.98 | (0.02) | 1.96 | (0.03) | 3.37 | | 1.01 | (0.02) | 1.94 | (0.03) | 3.42 | (0.13) | 1.01 | (0.02) | 1.96 | (0.01) | 3.16 | (0.05) | 1.01 | (0.01) | 1.96 | (0.01) | 3.24 | (0.07) | 1.01 | (0.02) | 1.95 | (0.02) |
| Ti | 0.00 | (0.00) | 0.02 | (0.03) | 0.00 | (0.00) | 0.00 | (0.00) | 0.00 | (0.00) | 0.00 | | 0.00 | (0.00) | 0.00 | (0.00) | 0.00 | (0.00) | 0.00 | (0.00) | 0.00 | (0.00) | 0.00 | (0.00) | 0.00 | (0.00) | 0.00 | (0.00) | 0.00 | (0.00) | 0.00 | (0.00) | 0.00 | (0.00) |
| Al | 0.06 | (0.02) | 1.36 | (0.05) | 0.00 | (0.00) | 0.07 | (0.01) | 0.08 | (0.04) | 1.41 | | 0.01 | (0.00) | 0.10 | (0.01) | 1.42 | (0.14) | 0.00 | (0.00) | 0.09 | (0.00) | 1.70 | (0.06) | 0.00 | (0.00) | 0.10 | (0.01) | 1.57 | (0.09) | 0.00 | (0.00) | 0.10 | (0.01) |
| Cr | 0.01 | (0.00) | 0.05 | (0.01) | 0.00 | (0.00) | 0.01 | (0.00) | 0.01 | (0.00) | 0.06 | | 0.00 | (0.00) | 0.01 | (0.00) | 0.08 | (0.01) | 0.00 | (0.00) | 0.00 | (0.00) | 0.06 | (0.01) | 0.00 | (0.00) | 0.01 | (0.00) | 0.06 | (0.01) | 0.00 | (0.00) | 0.01 | (0.00) |
| Fe | 0.10 | (0.01) | 0.20 | (0.03) | 0.10 | (0.01) | 0.09 | (0.01) | 0.12 | (0.01) | 0.22 | | 0.12 | (0.02) | 0.10 | (0.01) | 0.22 | (0.00) | 0.12 | (0.03) | 0.10 | (0.01) | 0.24 | (0.02) | 0.09 | (0.02) | 0.10 | (0.01) | 0.25 | (0.01) | 0.09 | (0.01) | 0.11 | (0.02) |
| Ni | 0.01 | (0.00) | 0.01 | (0.00) | 0.01 | (0.00) | 0.00 | (0.00) | 0.01 | (0.00) | 0.01 | | 0.00 | (0.00) | 0.00 | (0.00) | 0.01 | (0.00) | 0.00 | (0.00) | 0.00 | (0.00) | 0.01 | (0.00) | 0.00 | (0.00) | 0.00 | (0.00) | 0.01 | (0.01) | 0.00 | (0.00) | 0.00 | (0.00) |
| Mn | 0.00 | (0.00) | 0.00 | (0.00) | 0.00 | (0.00) | 0.00 | (0.00) | 0.00 | (0.00) | 0.00 | | 0.00 | (0.00) | 0.00 | (0.00) | 0.00 | (0.00) | 0.00 | (0.00) | 0.01 | (0.00) | 0.00 | (0.00) | 0.00 | (0.00) | 0.00 | (0.00) | 0.00 | (0.00) | 0.00 | (0.00) | 0.00 | (0.00) |
| Mg | 2.65 | (0.03) | 4.86 | (0.09) | 1.86 | (0.06) | 1.84 | (0.04) | 2.64 | (0.03) | 4.81 | | 1.83 | (0.03) | 1.85 | (0.04) | 4.67 | (0.07) | 1.84 | (0.04) | 1.83 | (0.01) | 4.79 | (0.04) | 1.88 | (0.03) | 1.83 | (0.01) | 4.81 | (0.06) | 1.86 | (0.04) | 1.82 | (0.00) |
| Ca | 0.00 | (0.00) | 0.01 | (0.01) | 0.00 | (0.00) | 0.00 | (0.00) | 0.00 | (0.00) | 0.00 | | 0.00 | (0.00) | 0.00 | (0.00) | 0.00 | (0.00) | 0.00 | (0.00) | 0.00 | (0.00) | 0.00 | (0.00) | 0.00 | (0.00) | 0.00 | (0.00) | 0.00 | (0.01) | 0.00 | (0.00) | 0.00 | (0.00) |
| O | 6.82 | (0.00) | 14.00 | (0.00) | 4.00 | (0.00) | 6.00 | (0.00) | 6.82 | (0.00) | 14.00 | | 4.00 | (0.00) | 6.00 | (0.00) | 14.00 | (0.00) | 4.00 | (0.00) | 6.00 | (0.00) | 14.00 | (0.00) | 4.00 | (0.00) | 6.00 | (0.00) | 14.00 | (0.00) | 4.00 | (0.00) | 6.00 | (0.00) |
| XMg | 0.96 | 0.02 | 0.96 | 0.06 | **0.95** | 0.05 | **0.95** | 0.05 | 0.96 | 0.04 | 0.96 | | 0.94 | 0.09 | 0.95 | 0.02 | 0.95 | 0.01 | 0.94 | 0.13 | 0.95 | 0.05 | 0.95 | 0.03 | 0.95 | 0.12 | 0.95 | 0.03 | 0.95 | 0.02 | 0.96 | 0.06 | 0.94 | 0.10 |
| XFe | 0.04 | 0.02 | 0.04 | 0.06 | 0.05 | 0.05 | 0.05 | 0.05 | 0.04 | 0.04 | 0.04 | | 0.06 | 0.09 | 0.05 | 0.02 | 0.05 | 0.01 | 0.06 | 0.13 | 0.05 | 0.05 | 0.05 | 0.03 | 0.05 | 0.12 | 0.05 | 0.03 | 0.05 | 0.02 | 0.04 | 0.06 | 0.06 | 0.10 |
| **KdFe-Mg Ol/En**[1] | **1.05** | | | | | | | | **1.13** | | | | | | | | **1.19** | | | | | | **0.87** | | | | | | **0.78** | | | | | |

**Table 3** (continued)

| Experiment | #262 | | | | | | #1273 | | | | #733 | | | | #735 | | | | #737 | | | |
|---|---|---|---|---|---|---|---|---|---|---|---|---|---|---|---|---|---|---|---|---|---|---|
| Mineral | Chl | | Ol | | En | | Ol | | En | | Ol | | En | | Ol | | En | | Ol | | En | |
| n | 5 | | 5 | | 4 | | 6 | | 7 | | 6 | | 2 | | 7 | | 3 | | 5 | | 4 | |
| SiO2 | 35.73 | (2.44) | 42.98 | (0.40) | 57.38 | (2.08) | 42.09 | (1.56) | 56.22 | (0.64) | 42.51 | (1.64) | 55.67 | (2.30) | 42.74 | (2.06) | 55.90 | (1.10) | 42.13 | (1.02) | 52.74 | (0.65) |
| TiO2 | 0.00 | (0.01) | 0.01 | (0.03) | 0.01 | (0.01) | 0.01 | (0.01) | 0.04 | (0.04) | 0.03 | (0.05) | 0.03 | (0.01) | 0.01 | (0.01) | 0.09 | (0.04) | 0.02 | (0.02) | 0.03 | (0.03) |
| Al2O3 | 14.50 | (1.87) | 0.22 | (0.14) | 3.06 | (1.24) | 0.22 | (0.20) | 3.51 | (0.44) | 0.10 | (0.09) | 2.89 | (0.84) | 0.18 | (0.23) | 4.99 | (0.86) | 0.21 | (0.17) | 3.45 | (0.56) |
| Cr2O3 | 0.97 | (0.33) | 0.15 | (0.10) | 0.27 | (0.05) | 0.16 | (0.08) | 0.34 | (0.12) | 0.12 | (0.07) | 0.28 | (0.06) | 0.11 | (0.11) | 0.25 | (0.04) | 0.15 | (0.11) | 0.34 | (0.01) |
| FeO | 2.91 | (0.27) | 3.29 | (0.36) | 2.65 | (0.12) | 5.55 | (0.65) | 4.39 | (0.83) | 5.69 | (0.97) | 4.41 | (0.20) | 10.18 | (0.75) | 4.83 | (0.56) | 10.18 | (1.66) | 5.86 | (0.30) |
| NiO | 0.20 | (0.04) | 0.39 | (0.16) | 0.20 | (0.07) | 0.30 | (0.03) | 0.08 | (0.04) | 0.39 | (0.13) | 0.17 | (0.00) | 0.00 | (0.00) | 0.00 | (0.00) | 0.88 | (1.12) | 0.18 | (0.02) |
| MnO | 0.03 | (0.03) | 0.09 | (0.03) | 0.08 | (0.02) | 0.08 | (0.04) | 0.10 | (0.03) | 0.13 | (0.03) | 0.10 | (0.05) | 0.10 | (0.03) | 0.11 | (0.04) | 0.11 | (0.04) | 0.15 | (0.01) |
| MgO | 33.64 | (0.34) | 53.54 | (1.40) | 37.05 | (0.93) | 51.54 | (1.47) | 35.52 | (0.50) | 52.03 | (0.51) | 36.30 | (1.07) | 48.03 | (0.77) | 34.86 | (0.15) | 47.92 | (1.10) | 36.80 | (1.71) |
| CaO | 0.01 | (0.01) | 0.03 | (0.02) | 0.03 | (0.03) | 0.01 | (0.02) | 0.01 | (0.01) | 0.01 | (0.01) | 0.09 | (0.01) | 0.01 | (0.01) | 0.03 | (0.05) | 0.02 | (0.02) | 0.05 | (0.03) |
| Total | 88.00 | (0.00) | 100.69 | (1.25) | 100.72 | (1.97) | 99.97 | (0.58) | 100.23 | (0.43) | 101.02 | (1.02) | 99.98 | (0.64) | 101.38 | (1.49) | 101.09 | (0.90) | 99.48 | (0.54) | 99.63 | (0.84) |
| Ions calculated on the basis of 14 oxygens for chlorite, 4 for olivine and 6 for orthopyroxene | | | | | | | | | | | | | | | | | | | | | | |
| Si | 3.31 | (0.21) | 1.01 | (0.01) | 1.93 | (0.03) | 1.01 | (0.03) | 1.92 | (0.02) | 1.01 | (0.02) | 1.91 | (0.06) | 1.03 | (0.03) | 1.89 | (0.02) | 1.01 | (0.02) | 1.84 | (0.03) |
| Ti | 0.00 | (0.00) | 0.00 | (0.00) | 0.00 | (0.00) | 0.00 | (0.00) | 0.00 | (0.00) | 0.00 | (0.00) | 0.00 | (0.00) | 0.00 | (0.00) | 0.00 | (0.00) | 0.00 | (0.00) | 0.00 | (0.00) |
| Al | 1.58 | (0.21) | 0.01 | (0.00) | 0.12 | (0.05) | 0.01 | (0.01) | 0.14 | (0.02) | 0.00 | (0.00) | 0.12 | (0.04) | 0.01 | (0.01) | 0.20 | (0.03) | 0.01 | (0.00) | 0.14 | (0.02) |
| Cr | 0.07 | (0.02) | 0.00 | (0.00) | 0.01 | (0.00) | 0.00 | (0.00) | 0.01 | (0.00) | 0.00 | (0.00) | 0.01 | (0.00) | 0.00 | (0.00) | 0.01 | (0.00) | 0.00 | (0.00) | 0.01 | (0.00) |
| Fe | 0.23 | (0.02) | 0.06 | (0.01) | 0.07 | (0.00) | 0.11 | (0.01) | 0.13 | (0.02) | 0.11 | (0.02) | 0.13 | (0.00) | 0.21 | (0.02) | 0.14 | (0.02) | 0.20 | (0.03) | 0.17 | (0.01) |
| Ni | 0.02 | (0.00) | 0.01 | (0.00) | 0.01 | (0.00) | 0.01 | (0.00) | 0.00 | (0.00) | 0.01 | (0.00) | 0.00 | (0.00) | 0.00 | (0.00) | 0.00 | (0.00) | 0.02 | (0.02) | 0.01 | (0.00) |
| Mn | 0.00 | (0.00) | 0.00 | (0.00) | 0.00 | (0.00) | 0.00 | (0.00) | 0.00 | (0.00) | 0.00 | (0.00) | 0.00 | (0.00) | 0.00 | (0.00) | 0.00 | (0.00) | 0.00 | (0.00) | 0.00 | (0.00) |
| Mg | 4.65 | (0.07) | 1.88 | (0.04) | 1.86 | (0.02) | 1.85 | (0.07) | 1.81 | (0.02) | 1.84 | (0.03) | 1.85 | (0.07) | 1.72 | (0.05) | 1.76 | (0.02) | 1.72 | (0.04) | 1.91 | (0.08) |
| Ca | 0.00 | (0.00) | 0.00 | (0.00) | 0.00 | (0.00) | 0.00 | (0.00) | 0.00 | (0.00) | 0.00 | (0.00) | 0.00 | (0.00) | 0.00 | (0.00) | 0.00 | (0.00) | 0.00 | (0.00) | 0.00 | (0.00) |
| O | 14.00 | (0.00) | 4.00 | (0.00) | 6.00 | (0.00) | 4.00 | (0.00) | 6.00 | (0.00) | 4.00 | | 6.00 | | 4.00 | | 6.00 | | 4.00 | | 6.00 | |
| XMg | 0.95 | 0.04 | 0.97 | 0.04 | 0.96 | 0.02 | 0.94 | 0.07 | 0.94 | 0.12 | 0.94 | | 0.94 | | 0.89 | | 0.93 | | 0.89 | | 0.92 | |
| XFe | 0.05 | 0.04 | 0.03 | 0.04 | 0.04 | 0.02 | 0.06 | 0.07 | 0.06 | 0.12 | 0.06 | | 0.06 | | 0.11 | | 0.07 | | 0.11 | | 0.08 | |
| **KdFe-Mg Ol/En** | **0.86** | | | | | | **0.87** | | | | **0.90** | | | | **1.53** | | | | **1.33** | | | |

**Table 3** (continued)

| Experiment | #739 | | | | | | #827 | | | | #830 | | | | #832 | | | | #860 | | | | #862 | | | |
|---|---|---|---|---|---|---|---|---|---|---|---|---|---|---|---|---|---|---|---|---|---|---|---|---|---|---|
| Mineral | Ol | | En | | Chl | | Ol | | En | | Ol | | En | | Ol | | En | | Ol | | En | | Ol | | En | |
| n | 4 | | 3 | | 2 | | 18 | | 4 | | 8 | | 12 | | 11 | | 7 | | 20 | | 5 | | 7 | | 6 | |
| SiO2 | 43.92 | (2.28) | 56.16 | (3.03) | 36.98 | (5.85) | 41.29 | (0.81) | 55.63 | (1.19) | 42.42 | (1.15) | 56.12 | (0.88) | 41.61 | (0.72) | 55.90 | (1.74) | 41.58 | (1.11) | 52.49 | (2.73) | 43.16 | (0.68) | 54.09 | (4.17) |
| TiO2 | 0.01 | (0.01) | 0.05 | (0.01) | 0.02 | (0.01) | 0.02 | (0.02) | 0.06 | (0.04) | 0.00 | (0.02) | 0.01 | (0.04) | 0.02 | (0.04) | 0.02 | (0.03) | 0.02 | (0.03) | 0.05 | (0.05) | 0.02 | (0.05) | 0.02 | (0.03) |
| Al2O3 | 0.13 | (0.09) | 2.74 | (1.21) | 12.06 | (1.67) | 0.13 | (0.11) | 4.44 | (0.83) | 0.22 | (0.20) | 3.41 | (0.48) | 0.13 | (0.07) | 3.90 | (0.81) | 0.18 | (0.16) | 4.47 | (0.72) | 0.05 | (0.05) | 2.15 | (0.83) |
| Cr2O3 | 0.14 | (0.04) | 0.24 | (0.05) | 0.85 | (0.19) | - | - | - | - | - | - | - | - | - | - | - | - | 0.10 | (0.12) | 0.00 | (0.00) | 0.08 | (0.07) | 0.25 | (0.10) |
| FeO | 5.62 | (0.59) | 3.17 | (1.20) | 3.32 | (0.19) | 8.57 | (2.89) | 3.84 | (0.50) | 6.42 | (0.29) | 4.27 | (0.21) | 6.89 | (1.51) | 4.36 | (0.68) | 8.00 | (0.52) | 4.27 | (0.75) | 4.32 | (0.93) | 4.05 | (1.75) |
| NiO | 0.00 | (0.00) | 0.00 | (0.00) | 0.00 | (0.00) | 0.30 | (0.06) | 0.19 | (0.02) | 0.28 | (0.09) | 0.08 | (0.02) | 0.32 | (0.08) | 0.16 | (0.05) | 0.39 | (0.06) | 0.13 | (0.05) | 0.37 | (0.05) | 0.22 | (0.10) |
| MnO | 0.15 | (0.04) | 0.09 | (0.08) | 0.04 | (0.01) | 0.11 | (0.04) | 0.08 | (0.02) | 0.11 | (0.03) | 0.14 | (0.03) | 0.11 | (0.02) | 0.10 | (0.02) | 0.11 | (0.02) | 0.08 | (0.05) | 0.12 | (0.03) | 0.09 | (0.01) |
| MgO | 52.54 | (2.54) | 36.58 | (4.89) | 35.53 | (4.24) | 49.34 | (2.15) | 34.96 | (0.53) | 50.98 | (0.93) | 35.63 | (1.04) | 50.34 | (1.48) | 35.79 | (1.14) | 49.06 | (1.15) | 32.31 | (2.16) | 54.27 | (0.75) | 41.04 | (3.50) |
| CaO | 0.01 | (0.02) | 0.03 | (0.02) | 0.06 | (0.03) | 0.00 | (0.02) | 0.08 | (0.08) | 0.01 | (0.02) | 0.07 | (0.17) | 0.02 | (0.04) | 0.02 | (0.03) | 0.01 | (0.02) | 0.22 | (0.24) | 0.00 | (0.03) | 0.02 | (0.02) |
| Total | 102.55 | | 99.28 | (7.66) | 89.36 | (12.00) | 99.77 | (0.87) | 99.27 | (1.54) | 100.44 | (1.27) | 99.73 | (0.66) | 99.44 | (1.29) | 100.25 | (0.87) | 99.45 | (1.12) | 94.02 | (5.49) | 102.39 | (0.91) | 101.93 | (1.22) |
| Ions calculated on the basis of 14 oxygens for chlorite, 4 for olivine and 6 for orthopyroxene | | | | | | | | | | | | | | | | | | | | | | | | | | |
| Si | 1.02 | (0.02) | 1.93 | (0.03) | 3.39 | (0.08) | 1.01 | (0.01) | 1.81 | (0.02) | 1.02 | (0.02) | 1.92 | (0.04) | 1.02 | (0.01) | 1.90 | (0.06) | 1.02 | (0.03) | 1.90 | (0.10) | 1.01 | (0.01) | 1.78 | (0.15) |
| Ti | 0.00 | (0.00) | 0.00 | (0.00) | 0.00 | (0.00) | 0.00 | (0.00) | 0.00 | (0.00) | 0.00 | (0.00) | 0.00 | (0.00) | 0.00 | (0.00) | 0.00 | (0.00) | 0.00 | (0.00) | 0.00 | (0.00) | 0.00 | (0.00) | 0.00 | (0.00) |
| Al | 0.00 | (0.00) | 0.11 | (0.05) | 1.30 | (0.01) | 0.00 | (0.00) | 0.18 | (0.03) | 0.01 | (0.01) | 0.14 | (0.02) | 0.00 | (0.00) | 0.16 | (0.03) | 0.01 | (0.01) | 0.19 | (0.03) | 0.00 | (0.00) | 0.08 | (0.03) |
| Cr | 0.00 | (0.00) | 0.01 | (0.00) | 0.06 | (0.01) | - | - | - | - | - | - | - | - | - | - | - | - | 0.00 | (0.00) | 0.00 | (0.00) | 0.00 | (0.00) | 0.00 | (0.00) |
| Fe | 0.11 | (0.02) | 0.09 | (0.03) | 0.25 | (0.03) | 0.18 | (0.06) | 0.11 | (0.01) | 0.13 | (0.01) | 0.12 | (0.01) | 0.12 | (0.04) | 0.12 | (0.02) | 0.17 | (0.01) | 0.13 | (0.02) | 0.09 | (0.02) | 0.11 | (0.05) |
| Ni | 0.00 | (0.00) | 0.00 | (0.00) | 0.00 | (0.00) | 0.01 | (0.00) | 0.01 | (0.00) | 0.01 | (0.00) | 0.00 | (0.00) | 0.01 | (0.00) | 0.00 | (0.00) | 0.01 | (0.00) | 0.00 | (0.00) | 0.01 | (0.00) | 0.01 | (0.00) |
| Mn | 0.00 | (0.00) | 0.00 | (0.00) | 0.00 | (0.00) | 0.00 | (0.00) | 0.00 | (0.00) | 0.00 | (0.00) | 0.00 | (0.00) | 0.00 | (0.00) | 0.00 | (0.00) | 0.00 | (0.00) | 0.00 | (0.00) | 0.00 | (0.00) | 0.00 | (0.00) |
| Mg | 1.83 | (0.03) | 1.87 | (0.12) | 4.86 | (0.11) | 1.80 | (0.06) | 1.79 | (0.03) | 1.83 | (0.02) | 1.81 | (0.04) | 1.84 | (0.06) | 1.81 | (0.05) | 1.80 | (0.03) | 1.76 | (0.08) | 1.89 | (0.02) | 2.01 | (0.16) |
| Ca | 0.00 | (0.00) | 0.00 | (0.00) | 0.01 | (0.00) | 0.00 | (0.00) | 0.00 | (0.00) | 0.00 | (0.00) | 0.00 | (0.01) | 0.00 | (0.00) | 0.00 | (0.00) | 0.00 | (0.00) | 0.01 | (0.01) | 0.00 | (0.00) | 0.00 | (0.00) |
| O | 4.00 | | 6.00 | | 14.00 | | 4.00 | (0.00) | 6.00 | (0.00) | 4.00 | (0.00) | 6.00 | (0.00) | 4.00 | (0.00) | 6.00 | (0.00) | 4.00 | (0.00) | 6.00 | (0.00) | 4.00 | (0.00) | 6.00 | (0.00) |
| XMg | 0.94 | | 0.95 | | 0.95 | | 0.91 | 0.03 | 0.94 | 0.01 | 0.93 | 0.00 | 0.94 | 0.01 | 0.89 | 0.05 | 0.94 | 0.01 | 0.92 | 0.01 | 0.93 | 0.01 | 0.96 | 0.01 | 0.95 | 0.02 |
| XFe | 0.06 | | 0.05 | | 0.05 | | 0.09 | 0.03 | 0.06 | 0.01 | 0.07 | 0.00 | 0.06 | 0.01 | 0.12 | 0.05 | 0.06 | 0.01 | 0.08 | 0.01 | 0.07 | 0.01 | 0.04 | 0.01 | 0.05 | 0.02 |
| **KdFe-Mg Ol/En** | **1.24** | | | | | | **1.59** | | | | **1.11** | | | | **1.90** | | | | **1.24** | | | | **0.82** | | | |

**Table 3** (continued)

| Experiment | #869 | | | | | | #897A | | | | #897B | | | | #900A | | | | #900B | | | |
|---|---|---|---|---|---|---|---|---|---|---|---|---|---|---|---|---|---|---|---|---|---|---|
| Mineral | Chl | | Ol | | En | | Ol | | En | | Ol | | En | | Ol | | En | | Ol | | En | |
| n | 7 | | 6 | | 4 | | 7 | | 5 | | 6 | | 3 | | 12 | | 10 | | 10 | | 8 | |
| SiO2 | 34.70 | (3.42) | 45.80 | (2.95) | 58.07 | (1.82) | 43.04 | (0.47) | 57.63 | (1.28) | 41.29 | (0.51) | 57.97 | (1.89) | 43.37 | (0.87) | 57.95 | (0.85) | 43.55 | (1.14) | 56.77 | (0.66) |
| TiO2 | -0.01 | (0.03) | 0.00 | (0.03) | 0.00 | (0.03) | 0.01 | (0.03) | 0.09 | (0.03) | 0.00 | (0.02) | 0.19 | (0.02) | 0.02 | (0.05) | 0.00 | (0.02) | 0.00 | (0.03) | 0.03 | (0.03) |
| Al2O3 | 8.94 | (2.45) | 0.29 | (0.20) | 1.65 | (0.47) | 0.12 | (0.09) | 4.97 | (0.49) | 0.06 | (0.05) | 4.89 | (0.25) | 0.06 | (0.08) | 2.76 | (0.27) | 0.13 | (0.19) | 3.13 | (0.30) |
| Cr2O3 | 0.57 | (0.16) | 0.13 | (0.04) | 0.26 | (0.12) | 0.08 | (0.12) | 0.51 | (0.11) | 0.05 | (0.02) | 0.82 | (0.14) | 0.06 | (0.09) | 0.12 | (0.06) | 0.05 | (0.05) | 0.17 | (0.07) |
| FeO | 2.15 | (0.11) | 2.62 | (0.65) | 3.48 | (0.84) | 3.90 | (0.09) | 2.39 | (0.10) | 9.92 | (1.01) | 5.31 | (0.52) | 2.88 | (0.81) | 4.12 | (0.42) | 4.05 | (0.68) | 5.26 | (0.70) |
| NiO | 0.29 | (0.04) | 0.36 | (0.16) | 0.13 | (0.05) | 0.32 | (0.03) | 0.08 | (0.02) | 0.33 | (0.05) | 0.07 | (0.03) | 0.37 | (0.05) | 0.14 | (0.02) | 0.36 | (0.02) | 0.14 | (0.02) |
| MnO | 0.05 | (0.02) | 0.11 | (0.03) | 0.12 | (0.03) | 0.10 | (0.03) | 0.08 | (0.03) | 0.13 | (0.04) | 0.10 | (0.02) | 0.11 | (0.03) | 0.10 | (0.04) | 0.09 | (0.02) | 0.11 | (0.03) |
| MgO | 30.45 | (3.88) | 50.96 | (3.40) | 37.26 | (1.58) | 53.22 | (0.73) | 36.80 | (1.25) | 48.62 | (0.70) | 35.82 | (1.60) | 55.28 | (1.30) | 36.80 | (0.39) | 53.32 | (1.01) | 35.71 | (0.64) |
| CaO | 0.16 | (0.21) | 0.03 | (0.02) | 0.02 | (0.03) | 0.01 | (0.02) | 0.04 | (0.01) | 0.01 | (0.02) | 0.07 | (0.05) | 0.02 | (0.02) | 0.01 | (0.03) | 0.01 | (0.01) | 0.03 | (0.03) |
| Total | 77.32 | (7.92) | 100.30 | (2.07) | 100.99 | (2.68) | 100.80 | (0.41) | 102.59 | (2.08) | 100.41 | (1.19) | 105.24 | (3.51) | 102.17 | (1.42) | 102.00 | (0.81) | 101.56 | (0.59) | 101.34 | (0.65) |
| Ions calculated on the basis of 14 oxygens for chlorite, 4 for olivine and 6 for orthopyroxene | | | | | | | | | | | | | | | | | | | | | | |
| Si | 5.19 | (0.27) | 1.10 | (0.08) | 1.96 | (0.04) | 1.02 | (0.02) | 1.91 | (0.00) | 1.01 | (0.00) | 1.94 | (0.01) | 1.01 | (0.02) | 1.96 | (0.03) | 1.37 | (0.04) | 1.46 | (0.02) |
| Ti | 0.00 | (0.00) | 0.00 | (0.00) | 0.00 | (0.00) | 0.00 | (0.00) | 0.00 | (0.00) | 0.00 | (0.00) | 0.01 | (0.00) | 0.00 | (0.00) | 0.00 | (0.00) | 0.00 | (0.00) | 0.00 | (0.00) |
| Al | 1.57 | (0.35) | 0.01 | (0.01) | 0.07 | (0.02) | 0.00 | (0.00) | 0.19 | (0.02) | 0.00 | (0.00) | 0.10 | (0.00) | 0.05 | (0.01) | 0.00 | (0.00) | 0.00 | (0.00) | 0.05 | (0.01) |
| Cr | 0.07 | (0.02) | 0.00 | (0.00) | 0.00 | (0.00) | 0.00 | (0.00) | 0.01 | (0.00) | 0.00 | (0.00) | 0.01 | (0.00) | 0.00 | (0.00) | 0.00 | (0.00) | 0.00 | (0.00) | 0.00 | (0.00) |
| Fe | 0.27 | (0.02) | 0.05 | (0.01) | 0.10 | (0.02) | 0.08 | (0.00) | 0.07 | (0.00) | 0.20 | (0.02) | 0.15 | (0.02) | 0.06 | (0.02) | 0.11 | (0.01) | 0.11 | (0.02) | 0.11 | (0.02) |
| Ni | 0.04 | (0.01) | 0.01 | (0.00) | 0.00 | (0.00) | 0.01 | (0.00) | 0.00 | (0.00) | 0.01 | (0.00) | 0.00 | (0.00) | 0.01 | (0.00) | 0.00 | (0.00) | 0.01 | (0.00) | 0.00 | (0.00) |
| Mn | 0.01 | (0.00) | 0.00 | (0.00) | 0.00 | (0.00) | 0.00 | (0.00) | 0.00 | (0.00) | 0.00 | (0.00) | 0.00 | (0.00) | 0.00 | (0.00) | 0.00 | (0.00) | 0.00 | (0.00) | 0.00 | (0.00) |
| Mg | 6.77 | (0.34) | 1.83 | (0.09) | 1.87 | (0.07) | 1.89 | (0.02) | 1.81 | (0.02) | 1.78 | (0.02) | 1.79 | (0.02) | 1.92 | (0.01) | 1.86 | (0.04) | 2.51 | (0.04) | 1.37 | (0.02) |
| Ca | 0.02 | (0.03) | 0.00 | (0.00) | 0.00 | (0.00) | 0.00 | (0.00) | 0.00 | (0.00) | 0.00 | (0.00) | 0.00 | (0.00) | 0.00 | (0.00) | 0.00 | (0.00) | 0.00 | (0.00) | 0.00 | (0.00) |
| O | 14.00 | (0.00) | 4.00 | (0.00) | 6.00 | (0.00) | 4.00 | (0.00) | 6.00 | (0.00) | 4.00 | (0.00) | 6.00 | (0.00) | 4.00 | (0.00) | 6.00 | (0.00) | 4.00 | (0.00) | 6.00 | (0.00) |
| XMg | 0.96 | 0.00 | 0.97 | 0.01 | 0.95 | 0.01 | 0.96 | 0.00 | 0.97 | 0.00 | 0.90 | 0.01 | 0.92 | 0.01 | 0.97 | 0.01 | 0.94 | 0.01 | 0.96 | 0.01 | 0.92 | 0.01 |
| XFe | 0.04 | 0.00 | 0.03 | 0.01 | 0.05 | 0.01 | 0.04 | 0.00 | 0.04 | 0.00 | 0.10 | 0.01 | 0.08 | 0.01 | 0.03 | 0.01 | 0.06 | 0.01 | 0.04 | 0.01 | 0.08 | 0.01 |
| **KdFe-Mg Ol/En** | | | **0.55** | | | | **1.12** | | | | **1.38** | | | | **0.47** | | | | **0.52** | | | |

**Table 4** Example of compositions of oxide minerals from EPMA

| Exp. Number | #1111 | | #1070 | | | | #1110 | | | | | #1224 | | | #1228 | | | #827 | | | #832 | | | #862 | | | #869 | | |
|---|---|---|---|---|---|---|---|---|---|---|---|---|---|---|---|---|---|---|---|---|---|---|---|---|---|---|---|---|---|
| Mineral nbr points | Mg 10 | Hem 4 | Mg 7 | Chr 1 | Hem 3 | Mg 9 | Chr 4 | SP 1 | Hem 9 | Mg 9 | Hem 11 | Mg 16 | Hem 1 | Chr 5 | SP 3 | Chr 4 | Mg 5 | Hem 4 | Chr 2 | SP 1 | Hem 7 | Mg 3 | | | | | | | | |
| Fe | 2.88 | 1.96 | 2.81 | 1.81 | 1.94 | 2.84 | 1.79 | 0.66 | 1.96 | 2.68 | 1.97 | 2.94 | 1.94 | 1.87 | 0.64 | 1.85 | 2.75 | 1.92 | 1.58 | 0.26 | 1.97 | 2.71 | 0.44 | | | | | | | |
| Mg | 0.08 | 0.01 | 0.12 | 0.06 | 0.01 | 0.03 | 0.10 | 0.39 | 0.00 | 0.28 | 0.00 | 0.01 | 0.01 | 0.10 | 0.96 | 0.09 | 0.15 | 0.01 | 0.58 | 0.79 | 0.02 | 0.20 | 0.12 | | | | | | | |
| Al | 0.00 | 0.00 | 0.00 | 0.01 | 0.00 | 0.01 | 0.03 | 0.93 | 0.00 | 0.01 | 0.00 | 0.00 | 0.00 | 0.02 | 0.19 | 0.02 | 0.02 | 0.04 | 0.18 | 1.13 | 0.00 | 0.01 | 0.00 | | | | | | | |
| Cr | 0.04 | 0.03 | 0.06 | 0.98 | 0.04 | 0.11 | 0.95 | 0.04 | 0.03 | 0.03 | 0.02 | 0.04 | 0.05 | 0.84 | 0.10 | 0.90 | 0.06 | 0.02 | 0.59 | 0.80 | 0.01 | 0.03 | 0.03 | | | | | | | |
| Mn | 0.00 | 0.00 | 0.01 | 0.10 | 0.00 | 0.01 | 0.09 | 0.01 | 0.00 | 0.00 | 0.00 | 0.00 | 0.00 | 0.09 | 0.20 | 0.45 | 0.18 | 0.01 | 0.04 | 0.00 | 0.00 | 0.01 | 0.00 | | | | | | | |
| Ti | 0.00 | 0.00 | 0.00 | 0.04 | 0.00 | 0.01 | 0.03 | 0.01 | 0.00 | 0.00 | 0.00 | 0.01 | 0.00 | 0.04 | 0.58 | 0.80 | 0.01 | 0.00 | 0.00 | 0.00 | 0.00 | 0.00 | 0.00 | | | | | | | |
| Cations sum | 3.00 | 2.00 | 3.00 | 3.00 | 2.00 | 3.00 | 3.00 | 3.00 | 2.00 | 3.00 | 2.00 | 3.00 | 2.00 | 3.00 | 3.00 | 3.00 | 3.00 | 2.00 | 3.00 | 3.00 | 2.00 | 3.00 | 3.00 | | | | | | | |

*Mg* Magnetite, *Hem* Hematite, *SP* Spinel, *Chr* Chromite

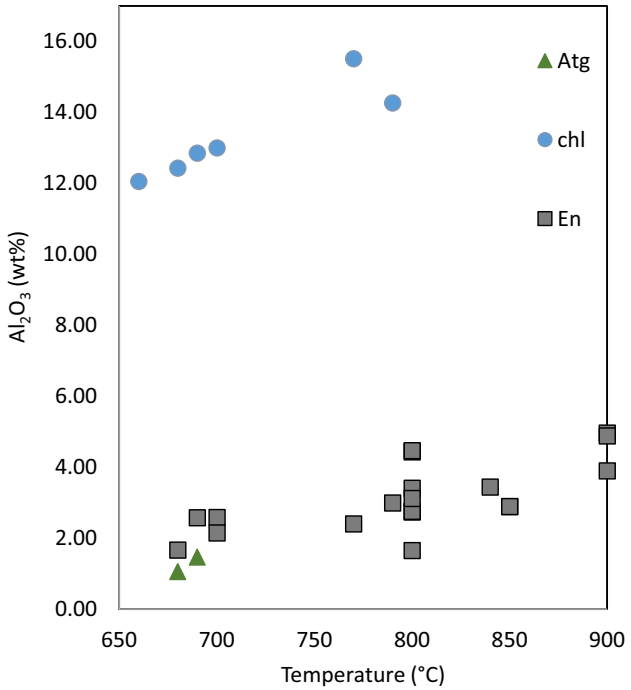


**Fig. 4** Evolution of concentration in $Al_2O_3$ wt.% in silicates (antigorite, chlorite and enstatite) as a function of experimental temperature from this study

the dehydration products olivine + enstatite resulting from a preliminary experiment at high pressure and high temperature. Their work suggests a temperature of antigorite stability up to 690 °C at 3 GPa (see Fig. 2a). Later on, Wunder and Schreyer (1997) first performed dehydration experiments on a synthetic antigorite gel in the MgO-$SiO_2$-$H_2O$ system, then mixed the reaction products olivine + enstatite with natural antigorite powder in a 1:1 ratio and added ~ 20 wt.% $H_2O$. These experiments constrain the stability limit of antigorite (0.68 wt.% $Al_2O_3$, 1.66 wt.% FeO in the bulk) around 640 °C at 2.8 GPa and 650 °C at 3.5 GPa. Bromiley and Pawley (2003) bracketed the destabilization of antigorite at 3 GPa between 620 and 660 °C for experiments in the MgO-$SiO_2$-$H_2O$ (MSH) system with 0.10 wt.% $Al_2O_3$ and 0.30 wt.% FeO (natural antigorite with synthetic olivine + synthetic enstatite + 20 wt.% water) and between 660 and 700 °C in the MgO-$Al_2O_3$-$SiO_2$-$H_2O$ (MASH) system with 3.06 wt.% $Al_2O_3$ and 5.47 wt.% FeO (natural antigorite with synthetic olivine + enstatite + chlorite + 20 wt.% water). Similar experiments were conducted by Padrón-Navarta et al. (2010a) and show that complete dehydration of serpentine from Cerro del Almirez (3.10 wt.% $Al_2O_3$ and 6.56 wt% FeO) occurred between 665 and 680 °C and 2.5—1.9 GPa. These experimental studies have highlighted the thermal stabilizing effect of Al in Atg. On the other hand, it has been suggested that the incorporation of iron reduces the thermal stability field of antigorite. Indeed, Merkulova

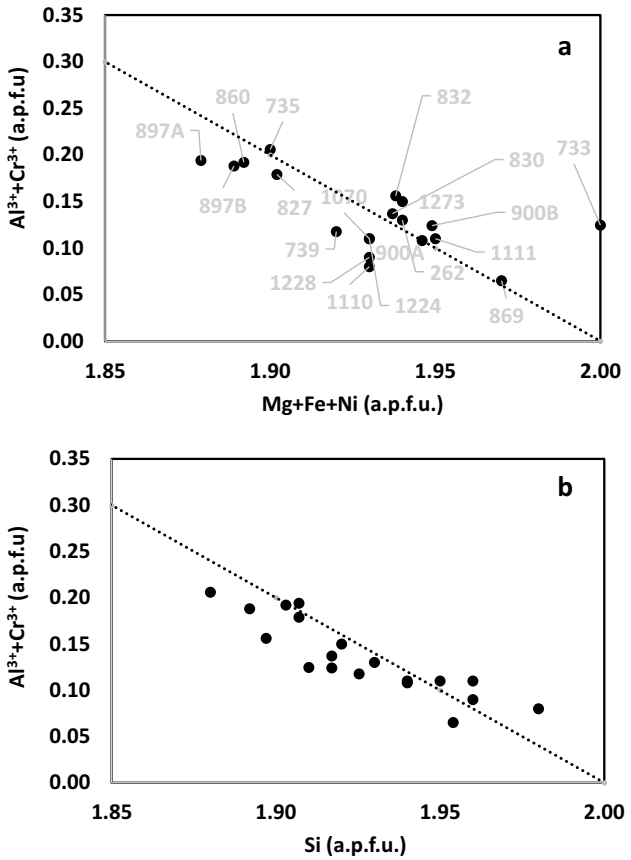


**Fig. 5** **a** Al + Cr content expressed in atoms per formula unit (a.p.f.u.) in orthopyroxene as a function of Mg + Fe + Ni content (a.p.f.u). The gray labels refer to the experiment number (see Table 2). **b** Al content (a.p.f.u.) in orthopyroxene as a function of Si content (a.p.f.u). The dashed line represents the theoretical Al Tschermack substitution in the tetrahedral site (e.g., 2(Al + Cr) = Mg + Fe + Ni + Si)

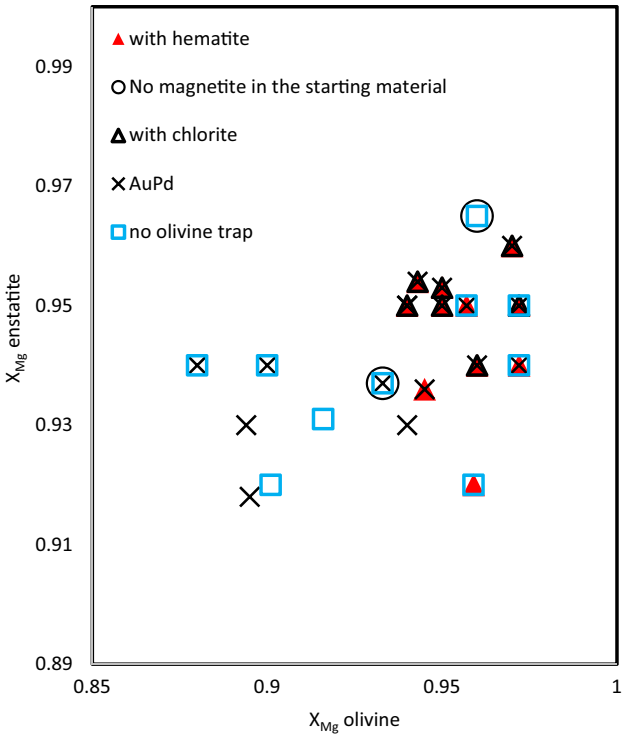


**Fig. 6** Dependence of $X_{Mg}$ of enstatite on $X_{Mg}$ of olivine and experimental conditions. The low-temperature experiments correspond to the chlorite-bearing samples

et al. (2016) have concluded that + 10 wt% FeO induced a decrease of about 25 °C for antigorite breakdown temperature, when compared to an iron-free system (i.e., 675 °C instead of 700 °C, at 2 GPa). In our study, we found that the dehydration of natural Atg-rich serpentinite containing 2.62 wt% FeO and 1.66 wt% $Al_2O_3$ occurs between 660 and 680 °C at 3 GPa (Fig. 2a). Thus, in agreement with previous thermal stability limits proposed for various Al- and Fe-bearing compositions representative of serpentinized mantle materials mentioned above (e.g., Bromiley and Pawley, 2003; Merkulova et al., 2016; Padrón-Navarta et al., 2010a; Ulmer and Trommsdorff, 1995).

## Open versus closed system

To perform hydrous experiments in a perfectly closed system is difficult. Actually, as long as $H_2$ is produced somewhere in the assembly, a gradient due to inhomogeneity in $H_2$ potential will force $H_2$ to diffuse in or out of the more or less permeable capsule. Therefore, a closed system can certainly not be maintained for a long time (see Truckenbrodt et al. 1997), and this is why we intended to keep the heating duration short (Table 2). Compared to the previous study of Merkulova et al. (2016), we do not observe disappearance of magnetite after antigorite starts dehydrating at low temperatures of 550 °C, but instead we observe the appearance of hematite. Magnetite in our experiments is stable up to ~ 800 °C. Given that our starting materials are similar (95% antigorite + 5% magnetite), the reasons for the different observations must arise from different experimental strategies. We used mainly $LaCrO_3$ furnace, $Au_{80}Pd_{20}$ capsule and short duration experiments instead of graphite furnace, Au capsule and long duration experiments in their case. We examine below the effect of changing these three parameters on the parageneses obtained in our study.

### i-Effect of the furnace material

We have monitored the oxygen fugacity imposed by the $LaCrO_3$ furnace in one experiment performed at 800 °C and 3 GPa. The value of oxygen fugacity is around QFM, showing that the $f_{O2}$ imposed by the furnace is lower than that of the sample, around QFM + 3 to + 4. This means that

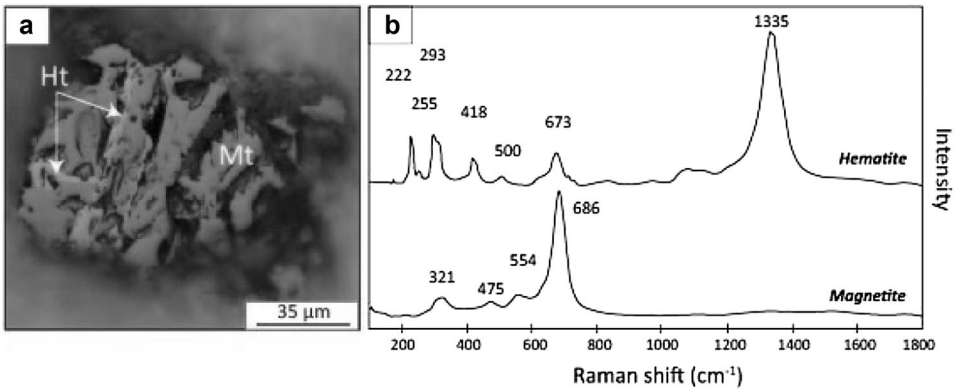


**Fig. 7** **a** Optical microscopy photograph in reflective light of a well-preserved magnetite partially transformed into hematite after antigorite dehydration, at 690 °C (#1110); **b** Corresponding Raman spectra of hematite and magnetite

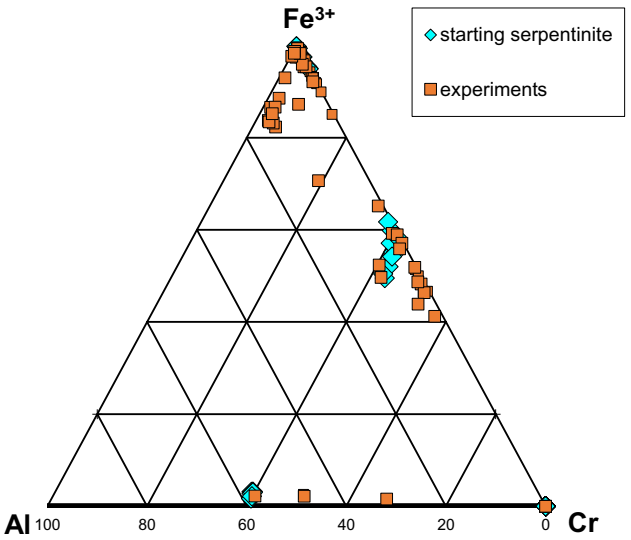


**Fig. 8** Ternary diagram showing the composition of the spinel oxides

the oxygen fugacities observed here are intrinsic of the serpentinite sample.

We have also performed two experiments using C furnace, at 700 and 900 °C. None display hematite. By comparison, when using the $LaCrO_3$ furnace at 700 °C and otherwise identical conditions hematite is observed. As discussed by Merkulova et al. (2017), the use of a graphite furnace in their experiments buffers the oxygen fugacity at ΔQFM-2, thus inhibiting the formation of hematite. The multi-anvil assembly used here is fired at 1000 °C prior to loading the capsule, so it should be relatively dry, thus limiting $H_2$ diffusion from the outer part of the assembly towards the sample. However, we should not discard the possibility that graphite diffuses from the furnace into the capsule, leading to the reduction of the sample through the reaction below as evidenced in piston-cylinder assemblies (see Matjuschkin et al. 2015):

$$2\,Fe_2O_3 sample + C = 4\,FeO sample + CO_2 \quad (7)$$

This reaction might explain why the use of a graphite furnace inhibits the formation of hematite either during long or short duration experiments. It also suggests that destabilization of magnetite can occur prematurely. Thermodynamic modeling indicates that magnetite is stable upon dehydration of antigorite (Piccoli et al. 2019), in agreement with the observation in nature of magnetite in partially dehydrated serpentinite in the Alps (Debret et al. 2014) or in Cerro del Almirez (Debret et al. 2015). In our case, magnetite is stable up to 800 °C, probably controlled by the stability of chlorite.

### ii- Effect of the capsule material

We examined the effect of the capsule material, by performing some experiments using Au in addition to those in $Au_{80}Pd_{20}$ (see Table 2). The oxygen fugacity prevailing within the capsule can be affected by the choice of the metal due to the different permeability to $H_2$ and solubility of Fe as a function of the composition of the metal. The implications are two-fold: first, if $H_2$ is lost by diffusion, excess oxygen will remain in the capsule, see reaction (8). Also, if iron is dissolved into the metal of the capsule, excess oxygen will be released in the sample, raising its oxygen fugacity see reaction (9):

$$H_2O = H_2 + {}^1\!/_2\,O_2 \quad (8)$$

$$FeO_{sample} = Fe_{alloy} + {}^1\!/_2\,O_2 \quad (9)$$

Since diffusion is a thermally activated process, we should expect that increasing temperature should enhance $H_2$ or Fe loss to the capsule, both leading to more oxidation of the sample. We observe that hematite coexists most of the time with chlorite, and is absent in the highest-temperature experiments, thus meaning that it is a low-temperature phase. Thus, we cannot explain hematite formation due to an experimental artifact leading to the opening of the system.

**Table 5** End member thermodynamic data used for calculating oxygen fugacity

| | ΔHf ° (298) (J/mol) | ST (J/K/mol) | Heat Capacity | | | | Vo ($m^3$/mol) | Ko (Pa) | α |
|---|---|---|---|---|---|---|---|---|---|
| | | | a (x1E3) | b (x1E-2) | c (x1E3) | d (x1E3) | | | |
| Fayalite | − 1,478,220 | 151 | 0.2011 | 1.733 | − 1960.6 | − 0.9009 | 4.63E-05 | 1.33E + 11 | 5.05E-05 |
| Forsterite | − 2,171,850 | 95.1 | 0.2333 | 0.1494 | − 603.8 | − 1.8697 | 4.37E-05 | 1.25E + 11 | 6.13E-05 |
| Enstatite | − 3,090,260 | 132.5 | 0.3562 | − 0.299 | − 596.9 | − 3.1853 | 6.26E-05 | 1.07E + 11 | 5.05E-05 |
| Ferrosilite | − 2,388,750 | 190.6 | 0,393 * | − 0.6579 | 1290.1 | − 4.058 | 6.59E-05 | 1.01E + 11 | 6.32E-05 |
| Hematite | − 825,730 | 87.4 | 0,17 * | 0 | − 2257.2 | − 0.6576 | 3.03E-05 | 2.00E + 11 | 5.99E-05 |
| Magnetite | − 1,115,550 | 146.1 | 0,28 * | − 0.7204 | − 1926.2 | − 1.6557 | 4.45E-05 | 1.85E + 11 | 6.96E-05 |
| $O_2$ | 0 | 205.15 | 0.0483 | − 0.0691 | 499.2 | − 0.4207 | | | |
| Quartz | − 910,880 | 41.5 | 0.1107 | − 0.5189 | 0.0 | − 1.1283 | 2.27E-05 | 7.50E + 10 | 6.50E-06 |

All data taken from Holland and Powell (1998), except a few Cp terms (*) that were modified to take into account for phase transitions, based on comparison with Perplex calculations. $Cp = a + bT + cT^{-2} + dT^{-0.5}$

A Murnaghan equation of state (like in Holland and Powell, 1998) is used to calculate $f_{O2}$ using Excell software

Activities were calculated assuming an ideal solid solution for pyroxene, and regular solid solution for olivine, whereby $a^{olivine}_{Mg2SiO4}$ and $a^{olivine}_{Fe2SiO4}$ are $X_{Mg}{}^2.\gamma_{Mg}$ and $X_{Fe}{}^2.\gamma_{Fe}$, respectively, with $X_{Fe} = Fe/(Fe + Mg)$ and the activity coefficients for olivine are determined from $RT \ln \gamma_a = W^{ol}(1\text{-}X_a)^2$ with $W^{ol} = 4200$ J/atom (Holland and Powell, 1998)

The activity coefficient in orthopyroxene is equal to 1

The activity coefficient for $Fe_2O_3$ in hematite is taken as unity as this phase was found to be very pure in composition (see Table 4)

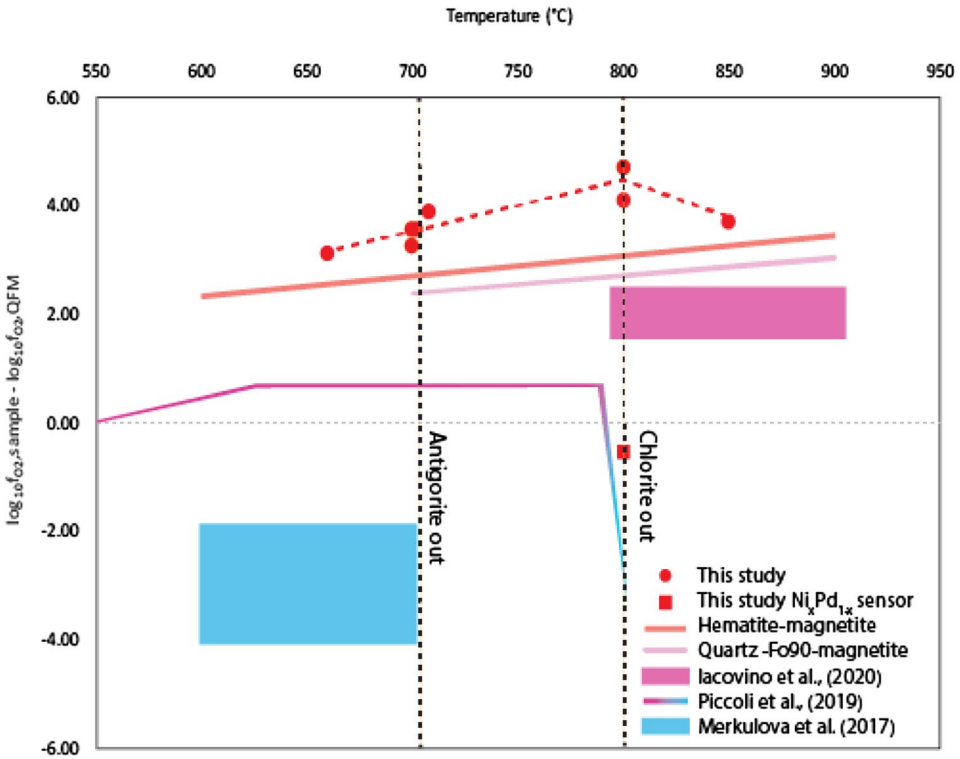


**Fig. 9** Oxygen fugacity relative to the Quartz–Fayalite–Magnetite (QFM) buffer of samples after antigorite dehydration, which contain hematite. Also shown is the Hematite–Magnetite (HM) equilibrium as the orange top line. Below it, the Quartz–Forsterite90–Magnetite equilibrium is shown as the pink line, and was calculated assuming $X_{Mg}{}^{olivine} = X_{Mg}{}^{orthopyroxene}$. The $f_{O2}$ reported in the experimental studies of Merkulova et al. (2017) and Iacovino et al. (2020) are shown as the blue and pink rectangles, respectively. While the thermodynamic model of Piccoli et al. (2019) is shown as the pink to blue line

Also, by comparing two samples synthesized in the same experiment but in different capsule material (#900A and #900B at 800 °C) we observe hematite in both capsules, and similar $X_{Mg}$ in olivine and orthopyroxene, therefore similar oxygen fugacity.

In addition, the measured profiles of Fe diffusion into $Au_{80}Pd_{20}$ or Au capsules evidence that a similar amount of iron is dissolved into both capsule materials (see Supplementary Fig. 3). Thus, both capsule materials seem to provide similar conditions to the samples.

### iii- Effect of heating duration

Our experiments are very short (5–24 h), especially in comparison to those of Merkulova et al. (2016) which lasted up to 9 days. In the more recent study of Iacovino et al. (2020), where experiments were performed at 800 °C, oxygen fugacity reaches stable values after 5 h of heating. In order to verify if equilibrium was reached in our samples, we performed experiments as a function of heating duration. Given the fine-grained texture of the dehydration products (see Fig. 3), the compositional changes of antigorite breakdown are accommodated rapidly, judging from the iron partitioning between olivine and enstatite close to 1 (see above). The kinetics of the oxide re-equilibration are more problematic as this phase is not neo-formed like chlorite, olivine and orthopyroxene, it requires more time to equilibrate. However, kinetics become crucial at temperatures above 800 °C, when magnetite is not stable, because dissolution into olivine and orthopyroxene is sluggish. Thus, counter-intuitively, experiments at low temperatures reach equilibrium faster than those at high temperature (above 800 °C) because magnetite is stable in low-temperature mineral assemblages.

Increasing the heating duration will improve the equilibration of the sample under temperature conditions where magnetite is not stable. The effect of heating duration on the decrease of $Kd_{Fe\text{-}Mg}{}^{Ol/Opx}$ was observed in both second and third series of experiments. With increasing heating duration from 5 h (#735) to 12 h (#737) at 840 °C, magnetite had time to completely disappear and get incorporated into the silicates, but the silicates still did not have time to completely homogenize and equilibrate. Indeed, the $Kd_{Fe\text{-}Mg}{}^{Ol/Opx}$ decreases from 1.5 to 1.3, converging to the equilibrium value of 1.1 (see Supplementary Fig. 1b). Also for samples, respectively, #832 and #827, $Kd_{Fe\text{-}Mg}{}^{Ol/Opx}$ decreases from 1.9 to 1.6 after heating at 800 °C and 12 h or 24 h of annealing, respectively.

### iv-Powder versus cored samples and effect of extra olivine trap

To test whether equilibrium was attained in the experiments using cylinders, we also used powdered samples. As shown in Table 2 and in Fig. 6, we observe no significant difference between the first series of experiments where serpentinite cylinder was used and the second and third series of experiments where powdered serpentinite was used. Especially, the presence of hematite is observed in both cored and powdered samples. This can be explained by the fact that after antigorite breakdown a similar grain size is achieved in both types of experiments, thus diffusion characteristic distances are similar for both types of starting materials.

As shown by samples of the second series (#737 with an olivine trap) compared to those of the third series (#827 and #832, without an olivine trap), magnetite seems to dissolve faster when in presence of the olivine trap. This suggests that the olivine trap made of Fo90 buffers the oxygen fugacity at lower values. The influence of the trap on the rest of the sample is made efficient by the saturation in fluid. The olivine trap can be considered as representative of the primary olivine that may coexist with antigorite + magnetite in a peridotite not fully serpentinized. As such, the first and second series of experiments, containing the olivine trap with $X_{Mg}$ of 0.90, are more representative of processes undergoing in partially hydrated peridotite, while the third series of experiments is more representative of what happens locally in a fully serpentinized peridotite.

To conclude about the open versus closed system, it seems that in this study, the system remained closed both because of the short duration of the experiments but also because the $LaCrO_3$ furnace seems to be inert with respect to $f_{O2}$. We can thus consider that the samples evolved controlled by their own, intrinsic, fugacity.

### Comparison with previous studies

We observe similar stability of natural serpentinite as in previous experimental studies, however we do observe the formation of hematite, which was never reported before. Hematite appears at the onset of antigorite dehydration and persists until 800–850 °C, often in coexistence with antigorite and/or chlorite (see Fig. 6). At 3 GPa, the oxygen fugacity of the samples increases with increasing temperature from 3.1 to 4.1 log units above QFM in the range of 680 to 800 °C (see Fig. 9). Then it seems to decrease to 3.7 at 850 °C. Higher $X_{Mg}$ in olivine and in orthopyroxene favors high oxygen fugacities in agreement with previous reports (Nitsan 1974). The destabilization of magnetite upon chlorite breakdown around 800 °C induces an increase of iron content in olivine and orthopyroxene, consequently causing a decrease in oxygen fugacity (see Eq. 2). Furthermore, thermodynamic modeling of Piccoli et al. (2019) predicts that upon chlorite breakdown, ~ 800 °C, the appearance of garnet should cause a stronger decrease in oxygen fugacity of 4 log units, from ΔQFM + 1 to ΔQFM -3 (see also Fig. 9). However, as already discussed, our starting material contains minute amounts of Ca and little Al, most of it being incorporated in orthopyroxene, causing a retardation of garnet formation.

The high oxygen fugacities observed in this study agree with the thermodynamic model of Evans and Powell (2015) between 650 and 850 °C for similar redox budgets (see Table 1). In contrast, the oxygen fugacities observed experimentally in this study are much higher than those proposed by Piccoli et al. (2019), between ΔQFM + 0.5 and ΔQFM + 1 between 625 and 775 °C, for a model peridotite

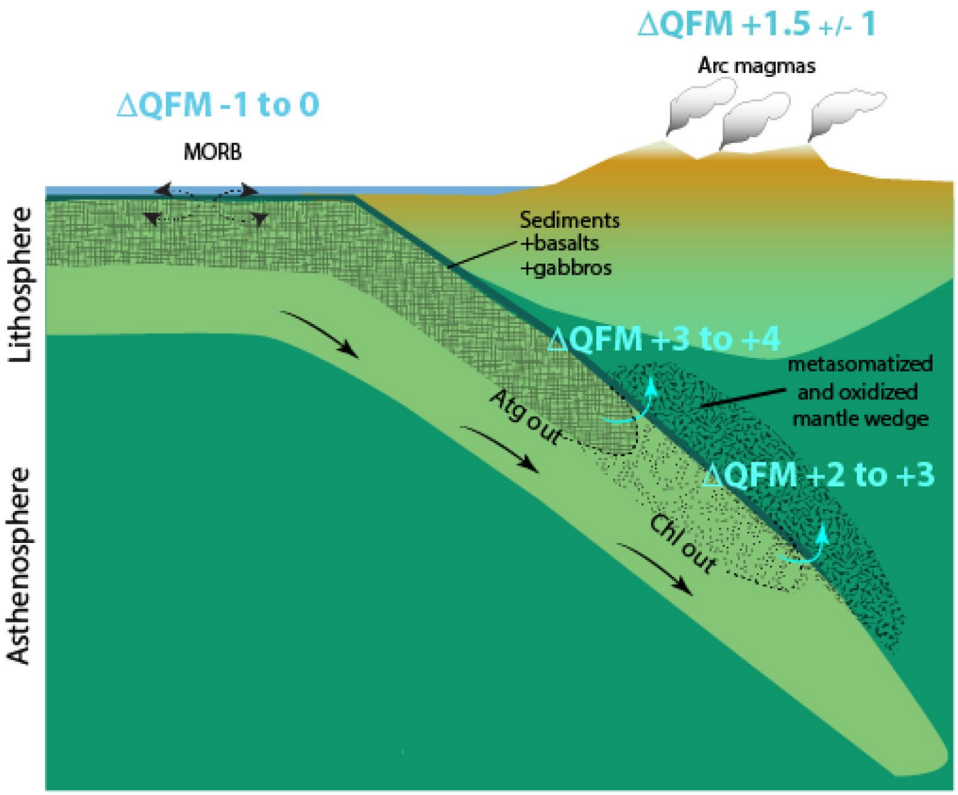


**Fig. 10** A model of subduction of the serpentinized mantle proposing a range of oxygen fugacity relative to the QFM buffer, for the released fluids following dehydration of antigorite and chlorite at higher pressures and temperatures. The oxygen fugacity ranges for MORB and arc magmas are from Bézos and Humler (2005), Cottrell and Kelley (2011), Berry et al. (2018) and from Kelley and Cottrell (2009, 2012), Brounce et al. (2014), Gaborieau et al. (2020), respectively

containing 12 wt.% of FeO (see Table 1 for starting compositions). In comparison, the serpentinite used in this study contains less than 8 wt.% FeO and this may be the reason for the higher oxygen fugacity values in the study of Piccoli et al. (2019): the higher the iron content in olivine and orthopyroxene the lower the oxygen fugacity (Nitsan, 1974).

Compared to previous experimental studies of antigorite dehydration, the oxygen fugacities found here for the post-antigorite parageneses are higher, with Δlog(QFM) of + 3 to + 4 at 3 GPa in the temperature range of 660–850 °C, than those found by Merkulova et al. (2017), Δlog(QFM) of − 2 to − 4 at 2 GPa and 550–700 °C. The pressure and temperature conditions are similar in both studies thus the difference in $f_{O2}$ recorded is most likely due to experimental design. As discussed above, an important difference between both studies is the buffering of oxygen fugacity: that is buffered at QFM-2 in an open system in the case of Merkulova et al. (2016), while in our case the oxygen fugacities recorded are intrinsic to the serpentinite system, which remained closed.

Finally, the oxygen fugacities reported here are higher than those measured by Iacovino et al. (2020), between ΔQFM + 1.5 and + 2.5 at 1 GPa and 800 °C using $Ni_xPd_{1-x}$ $f_{O2}$ sensor. For 900 °C, they measure ΔQFM + 2.5, which is close to that of our sample made at 850 °C, i.e. ΔQFM + 3.7. Note that our starting material has a higher redox budget of 0.24, compared to that of Iacovino et al. (2020), 0.14, see Table 1.

## Natural evidences for fluids with high redox budget

Reports on arc magmas indicate values of $Fe^{3+}/Fe_{total}$ that are higher (0.18—0.32; Kelley and Cottrell 2009, 2012; Gaborieau et al. 2020) than in MORBs (0.13—0.17, Bézos and Humler 2005; Cottrell and Kelley 2011; Berry et al. 2018), and which are furthermore positively correlated with water contents in melt inclusions (Kelley and Cottrell 2009; Gaborieau et al. 2020). Estimates of the oxygen fugacity at which the melts equilibrated yield ΔQFM ~ 1.5 ± 1 (Carmichael 1991; Kelley and Cottrell 2009; 2012; Brounce et al. 2014). Estimates of $f_{O2}$ in the mantle wedge above subduction zones as inferred from the ferric/ferrous ratio of iron in spinel peridotites xenoliths (Brandon and Draper 1996; Parkinson and Arculus 1999; Bénard et al. 2018) and mineral assemblages in basic lavas (Carmichael 1991) also yield values ranging from QFM + 1 to QFM + 2. A similar range is reported for orogenic garnet-bearing peridotites from the Sulu Belt or the Alps, thought to be representative of the metasomatized mantle wedge (Malaspina et al. 2009). Even more oxidized examples are found in subduction zone mélanges representing the slab-mantle interface, with extremely high values of oxygen fugacity ΔQFM + 12 (at 1 bar, e.g., Tumiati et al. 2015).

However, the question of whether or not these evidences relate to the redox state of the source of arc magmas is still an ongoing debate. The V/Sc and Zn/Fe systematics in MOR

and arc basalts display similarities, which indicate that they formed under similar conditions of oxygen fugacity near QFM (Lee et al. 2005, 2010; Mallmann and O'Neill 2009). If this is the case, then the oxidized character of arc magmas must be explained by differentiation in the crust or by degassing of sulfur (Burgisser and Scaillet 2007). However, so far, evidences for effects of crystallization of olivine (sink of $Fe^{2+}$) or magnetite (sink of $Fe^{3+}$) on the $Fe^{3+}$/Fe ratios of arc glasses are lacking (Brounce et al. 2014).

In this study, we show that fluids forming due to antigorite dehydration are equilibrated at high oxygen fugacities of $\Delta$QFM + 2 to + 4 (see Fig. 10). To expel such highly oxidized fluids from the slab could explain the higher redox state of arc magmas compared to MORB. These fluids can communicate their redox potential either via solutes of variable valences such as sulfur or carbon (as proposed by Merkulova et al. 2017). However, these are present in small amounts in the serpentinized mantle that subducted to sub-arc conditions (Debret et al. 2016b; Alt et al. 2013). An alternative model (see reaction below) was proposed by Iacovino et al. (2020) whereby the redox potential is transferred by electrons in the fluid which can exchange infinitely with the iron- or transition-element -bearing rocks through which the fluid travels (Tumiati et al. 2015).

$$2Fe^{2+}_{solid} + 2\,H^{+}_{aqueous} \leftrightarrow 2Fe^{3+}_{solid} + H_{2\,aqueous} \quad (10)$$

The change occurring in the physical and chemical properties of water at around 3 GPa and 600–800 °C, which leads to a more ionic liquid as suggested by previous studies (e.g., Bureau and Keppler 1999; Till et al. 2012), probably facilitates such reaction.

Of course, that the fluids can carry a high redox potential does not mean that they actually do across the entire subduction zone. Evidences that fluids do transfer a high redox potential exist in mafic high-pressure rocks representing subducting lithosphere. For example, Philippot and Selverstone (1991) report the presence of anhydrite ($CaSO_4$) and hematite in fluid inclusions within omphacites in eclogites from the Alps, but anhydrite co-existing with pyrite seems to be common to many inclusions worldwide (Frezzotti and Ferrando 2015). Still, the picture is probably more complicated as evidences for reduced fluids also exist in the form of $CH_4$ inclusions (Song et al. 2009), precipitation of graphite (Malvoisin et al. 2012; Galvez et al. 2013) or sulfide veins (Li et al. 2020).

## Conclusion

By performing experiments at 3 GPa and 600 to 900 °C, we have reproduced the different stages of prograde high-pressure dehydration of natural antigorite + magnetite assemblage. The new paragenesis contains secondary antigorite, chlorite, olivine, orthopyroxene and a fluid phase. Despite difference in Al and Fe content, we find similar phase boundaries as previously reported, however, we observe the formation of hematite that was not reported before. Hematite is observed concomitantly with high $X_{Mg}$ in olivine, of 0.94–0.97, generally at low temperatures, below 800 °C, in coexistence with chlorite. The $X_{Mg}$ of silicates decreases at higher temperatures once chlorite is destabilized and magnetite breakdown starts. The oxygen fugacity of the samples ranges between 3.1 and 4.1 log units above QFM, and increases with increasing temperature in the chlorite stability field but then decreases above chlorite breakdown around 800 °C.

We tested the effect of our experimental strategy on the phase equilibria by varying: (i) furnace material (lanthanum chromite versus graphite), (ii) capsule material, (iii) heating duration and (iv) presence of an olivine trap. We can reasonably conclude that the antigorite dehydration proceeds in our experiments in a closed system, principally because of the use of chromite furnace that is relatively inert, and because of the short heating durations that limit the loss or gain of $H_2$. Especially we find that the addition of a San Carlos olivine trap (with Fo90 composition) accelerates magnetite disappearance by driving down the oxygen fugacity of the entire system thanks to an efficient fluid transport.

We thus confirm that serpentine dehydration releases fluids equilibrated at a very high oxygen fugacity. Such high $f_{O2}$will induce sulfur oxidation into sulfate as proposed in numerical models (Debret and Sverjensky 2017). Fluids with such an oxidizing potential have strong consequences on the mantle wedge physical and chemical properties (through $SO_4^{2-}{}_{(aq)}$ transport or electron transport) and consequently on the oxidation state of the source of arc magmas. The oxidizing character of the antigorite breakdown reaction and of the associated fluids could thus be a relevant explanation of the high oxidation state of arc magmas compared to MORBs (Kelley and Cottrell 2009; Gaborieau et al. 2020).

**Acknowledgements** We thank D. Mainprice for providing the natural sample of serpentinite which was used as starting material. We are grateful to Kayla Iacovino and an anonymous reviewer for their very constructive comments, we warmly thank José-Alberto Padrón-Navarta for guidance in the thermodynamic calculations as well as in many other aspects, and Denis Andrault for his insight into our $f_{O2}$ calculations. This work was financed by the ANR HYDEEP "Hydrogen in the Deep Earth" project to N. Bolfan-Casanova and the ANR OxyDeep project to Denis Andrault. We also thank J.-L. Devidal, for his assistance during microprobe analysis; J.-M. Hénot for assistance with the SEM; J.-L. Fruquière and C. Guillot for machining the multi-anvil

parts; Claire Fonquernie for measuring the volatiles content using the elemental analyzer. This is Laboratory of Excellence Clervolc contribution number 433.

## References


Alt JC, Schwarzenbach EM, Früh-Green GL, Shanks WC, Bernasconi SM, Garrido CJ, Crispini L, Gaggero L, Padrón-Navarta JA, Marchesi C (2013) The role of serpentinites in cycling of carbon and sulfur: Seafloor serpentinization and subduction metamorphism. Lithos 178:40–54. https://doi.org/10.1016/J.LITHOS.2012.12.006

Andreani M, Daniel I, Pollet-Villard M (2013) Aluminum speeds up the hydrothermal alteration of olivine. Am Mineral 98:1738–1744

Ballhaus C, Berry RF, Green DH (1991) High-pressure experimental calibration of the olivine-ortho-rtho-pyroxene-spinel oxygen geobarometer- implication for the oxidation-state of the upper mantle. Contrib Mineral Petrol 107(1):27–40. https://doi.org/10.1007/bf00311183

Bean VE, Akimoto S, Bell PM, Block S, Holzapfel WB, Manghnani MH, Nicol MF, Stishov SM (1986) Another step toward an international practical pressure scale. Phys. B+C 139–140:52–54. https://doi.org/10.1016/0378-4363(86)90521-8

Benard A, Woodland AB, Arculus RJ, Nebel O, McAlpine SRB (2018) Variation in sub-arc mantle oxygen fugacity during partial melting recorded in refractory peridotite xenoliths from the West Bismarck Arc. Chem Geol 486:16–30. https://doi.org/10.1016/j.chemgeo.2018.03.004

Berry AJ, Stewart GA, O'Neill HSC, Mallmann G, Mosselmans JFW (2018) A re-assessment of the oxidation state of iron in MORB glasses. Earth Planet Sci Lett 483:114–123. https://doi.org/10.1016/j.epsl.2017.11.032

Bézos A, Humler E (2005) The $Fe^{3+}$/ΣFe ratios of MORB glasses and their implications for mantle melting. Geochim Cosmochim Acta 69:711–725. https://doi.org/10.1016/j.gca.2004.07.026

Bose K, Navrotsky A (1998) Thermochemistry and phase equilibria of hydrous phases in the system MgO-SiO2-H2O: Implications for volatile transport to the mantle. J Geophys Res 103:9713. https://doi.org/10.1029/98JB00506

Bliss NW, MacLean WH (1975) The paragenesis of zoned chromite from central Manitoba. Geochem Cosmochim Acta 39:973–990

Bureau H, Keppler H (1999) Complete miscibility between silicate melts and hydrous fluids in the upper mantle: experimental evidence and geochemical implications. Earth Planet Sci Lett 165:187–196. https://doi.org/10.1016/s0012-821x(98)00266-0

Burkhard D (1993) Accessory chromium spinels: Their coexistence and alteration in serpentinites. Geochem Cosmochim Acta 37:1297406

Burgisser A, Scaillet B (2007) Redox evolution of a degassing magma rising to the surface. Nature 445:194–197. https://doi.org/10.1038/nature05509

Brandon AD, Draper DS (1996) Constraints on the origin of the oxidation state of mantle overlying subduction zones: An example from Simcoe, Washington, USA. Geochim Cosmochim Acta 60:1739–1749. https://doi.org/10.1016/0016-7037(96)00056-7

Bretscher A, Hermann J, Pettke T (2018) The influence of oceanic oxidation on serpentinite dehydration during subduction. Earth Planet Sci Lett 499:173–184. https://doi.org/10.1016/j.epsl.2018.07.017

Bromiley GD, Pawley AR (2003) The stability of antigorite in the systems MgO-SiO2-H2O (MSH) and MgO-Al2O3-SiO2-H2O (MASH): The effects of $Al^{3+}$substitution on high-pressure stability. Am Mineral 88:99–108. https://doi.org/10.2138/am-2003-0113

Brounce MN, Kelley KA, Cottrell E (2014) Variations in $Fe^{3+}$/Fe of Mariana Arc Basalts and Mantle Wedge $fO_2$. J Petrol 55:2513–2536. https://doi.org/10.1093/petrology/egu065

Cannat M, Bideau D, Hébert R (1990) Plastic deformation and magmatic impregnation in serpentinized ultramafic rocks from the Garrett transform fault (East Pacific Rise). Earth Planet Sci Lett 101:216–232. https://doi.org/10.1016/0012-821X(90)90155-Q

Capitani G, Mellini M (2004) The modulated crystal structure of antigorite: the m = 17 polysome. Am Mineral 89:147–158

Carmichael ISE (1991) The redox states of basic and silicic magmas: a reflection of their source regions? Contrib to Mineral Petrol 106:129–141. https://doi.org/10.1007/BF00306429

Cottrell E, Kelley KA (2011) The oxidation state of Fe in MORB glasses and the oxygen fugacity of the upper mantle. Earth Planet Sci Lett 305:270–282. https://doi.org/10.1016/j.epsl.2011.03.014

de Faria DLA, Venâncio Silva S, de Oliveira MT (1997) Raman microspectroscopy of some iron oxides and oxyhydroxides. J Raman Spectrosc 28:873–878. https://doi.org/10.1002/(SICI)1097-4555(199711)28:11<873:AID-JRS177>3.0.CO;2-B

Debret B, Andreani M, Muñoz M, Bolfan-Casanova N, Carlut J, Nicollet C, Schwartz S, Trcera N (2014) Evolution of Fe redox state in serpentine during subduction. Earth Planet Sci Lett 400:206–218. https://doi.org/10.1016/j.epsl.2014.05.038

Debret B, Bolfan-Casanova N, Padrón-Navarta JA, Martin-Hernandez F, Andreani M, Garrido CJ, López Sánchez-Vizcaíno V, Gómez-Pugnaire MT, Muñoz M, Trcera N (2015) Redox state of iron during high-pressure serpentinite dehydration. Contrib Mineral Petrol 169:36. https://doi.org/10.1007/s00410-015-1130-y

Debret B, Millet M-A, Pons M-L, Bouilhol P, Inglis E, Williams H (2016a) Isotopic evidence for iron mobility during subduction. Geology 44:215–218. https://doi.org/10.1130/G37565.1

Debret B, Koga KT, Cattani F, Nicollet C, Van den Bleeken G, Schwartz S (2016b) Volatile (Li, B, F and Cl) mobility during amphibole breakdown in subduction zones. Lithos 244:165–181

Debret B, Sverjensky DA (2017) Highly oxidising fluids generated during serpentinite breakdown in subduction zones. Sci Rep 7:10351. https://doi.org/10.1038/s41598-017-09626-y

Deschamps F, Guillot S, Godard M, Chauvel C, Andreani M, Hattori K (2010) In situ characterization of serpentinites from forearc mantle wedges: Timing of serpentinization and behavior of fluid-mobile elements in subduction zones. Chem Geol 269:262–277. https://doi.org/10.1016/j.chemgeo.2009.10.002

Evans B, Johannes W, Oterdoom H, Trommsdorff V (1976) Stability of crystotile and serpentinite in the serpentine multisystem. Schweiz Mineral Petrogr Mitt 56:79–93

Evans BW, Trommsdorff V (1978) Petrogenesis of garnet lherzolite, Cima di Gagnone. Lepontine Alps Earth Planet Sci Lett 40:333–348. https://doi.org/10.1016/0012-821X(78)90158-9

Evans KA (2006) Redox decoupling and redox budgets: Conceptual tools for the study of earth systems. Geology 34:489–492

Evans KA (2012) The redox budget of subduction zones. Earth Sci Rev 113:11–32. https://doi.org/10.1016/j.earscirev.2012.03.003

Evans KA, Tomkins AG (2011) The relationship between subduction zone redox budget and arc magma fertility. Earth Planet Sci Lett 308:401–409

Evans KA, Powell R (2015) The effect of subduction on the sulphur, carbon and redox budget of lithospheric mantle. J Metamorph Geol 33:649–670

Frezzotti ML, Ferrando S (2015) The chemical behavior of fluids released during deep subduction based on fluid inclusions. Am Miner 100:352–377. https://doi.org/10.2138/am-2015-4933

Gaetani GA, Grove TL (1998) The influence of water on melting of mantle peridotite. Contrib to Mineral Petrol 131:323–346. https://doi.org/10.1007/s004100050396

Galvez ME, Beyssac O, Martinez I, Benzerara K, Chaduteau C, Malvoisin B, Malavieille J (2013) Graphite formation by carbonate reduction during subduction. Nat Geosci 6(6):473–477. https://doi.org/10.1038/ngeo1827

Garrido CJ, López Sánchez-Vizcaíno V, Gómez-Pugnaire MT, Trommsdorff V, Alard O, Bodinier J-L, Godard M (2005) Enrichment of HFSE in chlorite-harzburgite produced by high-pressure dehydration of antigorite-serpentinite: Implications for subduction magmatism. Geochem Geophys Geosystems. https://doi.org/10.1029/2004GC000791

Gaborieau M, Laubier M, Bolfan-Casanova N, McCammon CA, Vantelon D, Chumakov AI, Schiavi F, Neuville DR, Venugopal S (2020) Determination of $Fe^{3+}/\Sigma Fe$ of olivine-hosted melt inclusions using Mössbauer and XANES spectroscopy. Chem Geol 547:119646

Gervilla F, Padrón-Navarta JA, Kerestedjian T, Sergeeva I, González-Jiménez JM, Fanlo I (2012) Formation of ferrian chromite in podiform chromitites from the Golyamo Kamenyane serpentinite, Eastern Rhodopes, SE Bulgaria: A two-stage process. Contrib Mineral Petrol 164:643–657

Grove TL, Chatterjee N, Parman SW, Médard E (2006) The influence of $H_2O$ on mantle wedge melting. Earth Planet Sci Lett 249:74–89. https://doi.org/10.1016/j.epsl.2006.06.043

Guillot S, Hattori KH, de Sigoyer J (2000) Mantle wedge serpentinization and exhumation of eclogites: Insights from eastern Ladakh, northwest Himalaya. Geology 28:199. https://doi.org/10.1130/0091-7613(2000)28<199:MWSAEO>2.0.CO;2

Guillot S, Schwartz S, Reynard B, Agard P, Prigent C (2015) Tectonic significance of serpentinites. Tectonophysics 646:1–19

Hernlund J, Leinenweber K, Locke D, Tyburczy JA (2006) A numerical model for steady-state temperature distributions in solid-medium high-pressure cell assemblies. Am Mineral 91:295–305

Holland TJB, Powell R, Sciences E, Cb C (1998) An internally consistent thermodynamic data set for phases of petrological interest. J Metamorph Geol 16:309–343

Iacovino K, Guild MR, Till CB (2020) Aqueous fluids are effective oxidizing agents of the mantle in subduction zones. Contrib Mineral Petrol 175(4):21. https://doi.org/10.1007/s00410-020-1673-4

Kelley KA, Cottrell E (2012) The influence of magmatic differentiation on the oxidation state of Fe in a basaltic arc magma. Earth Planet Sci Lett 329–330:109–121. https://doi.org/10.1016/j.epsl.2012.02.010

Kelley KA, Cottrell E (2009) Water and the oxidation state of subduction zone magmas. Science 325:605–607. https://doi.org/10.1126/science.1174156

Klein F, Bach W, Humphris SE, Kahl WA, Jons N, Moskowitz B, Berquo TS (2014) Magnetite in seafloor serpentinite–Some like it hot. Geology 42:135–138

Lee CTA, Leeman WP, Canil D, Li ZXA (2005) Similar V/Sc systematics in MORB and arc basalts: Implications for the oxygen fugacities of their mantle source regions. J Petrol 46(11):2313–2336. https://doi.org/10.1093/petrology/egi056

Lee CTA, Luffi P, Le Roux V, Dasgupta R, Albaréde F, Leeman WP (2010) The redox state of arc mantle using Zn/Fe systematics. Nature 468(681–685):939. https://doi.org/10.1038/nature09617

Li J-L, Schwarzenbach EM, John T, Ague JJ, Huang F, Gao J, Klemd R, Whitehouse MJ, Wang X-S (2020) Uncovering and quantifying the subduction zone sulfur cycle from the slab perspective. Nat Commun 11(1):514. https://doi.org/10.1038/s41467-019-14110-4

López Sánchez-Vizcaíno V, Trommsdorff V, Gómez-Pugnaire MT, Garrido CJ, Müntener O, Connolly JAD (2005) Petrology of titanian clinohumite and olivine at the high-pressure breakdown of antigorite serpentinite to chlorite harzburgite (Almirez Massif, S. Spain). Contrib Mineral Petrol 149:627–646. https://doi.org/10.1007/s00410-005-0678-3

Malaspina N, Poli S, Fumagalli P (2009) The Oxidation State of Metasomatized Mantle Wedge: Insights from C-O-H-bearing Garnet Peridotite. J Petrol 50(8):1533–1552. https://doi.org/10.1093/petrology/egp040

Mallmann G, O'Neill HSC (2009) The Crystal/Melt Partitioning of V during Mantle Melting as a Function of Oxygen Fugacity Compared with some other Elements (Al, P, Ca, Sc, Ti, Cr, Fe, Ga, Y, Zr and Nb). J Petrol 50(9):1765–1794. https://doi.org/10.1093/petrology/egp053

Malvoisin B, Carlut J, Brunet F, (2012) Serpentinization of oceanic peridotites: 1. A high-sensitivity method to monitor magnetite production in hydrothermal experiments. J Geophys Res 117, B01104 Malaspina N, Poli S, Fumagalli P, (2009) The Oxidation State of Metasomatized Mantle Wedge: Insights from C-O-H-bearing Garnet Peridotite. J Petrol 50(8):1533–1552. https://doi.org/10.1093/petrology/egp040

Matjuschkin V, Brooker RA, Tattitch B, Blundy JD, Stamper CC (2015) Control and monitoring of oxygen fugacity in piston cylinder experiments. Contrib Mineral Petrol 169(1):16. https://doi.org/10.1007/s00410-015-1105-z

Maurice J, Bolfan-Casanova N, Padrón-Navarta JA, Manthilake G, Hammouda T, Hénot JM, Andrault D (2018) The stability of hydrous phases beyond antigorite breakdown for a magnetite-bearing natural serpentinite between 6.5 and 11 GPa. Contrib Mineral Petrol 173:86. https://doi.org/10.1007/s00410-018-1507-9

Mellini M, Trommsdorff V, Compagnoni R (1987) Antigorite polysomatism - behavior during progressive metamorphism. Contrib Mineral Petrol 97:147–155

Merkulova MV, Muñoz M, Vidal O, Brunet F (2016) Role of iron content on serpentinite dehydration depth in subduction zones: Experiments and thermodynamic modeling. Lithos. https://doi.org/10.1016/j.lithos.2016.09.007

Merkulova MV, Muñoz M, Brunet F, Vidal O, Hattori K, Vantelon D, Trcera N, Huthwelker T (2017) Experimental insight into redox transfer by iron- and sulfur-bearing serpentinite dehydration in subduction zones. Earth Planet Sci Lett 479:133–143. https://doi.org/10.1016/J.EPSL.2017.09.009

Mével C (2003) Serpentinization of abyssal peridotites at mid-ocean ridges. CR Geosci 335:825–852

Nitsan U (1974) Stability field of olivine qwith respect to oxidation and reduction. J Geoph Res 79:706–711. https://doi.org/10.1029/JB079i005p00706

O'Neill HSC (1987) The quartz-fayalite-iron and quartz-fayalite-magnetite equilibria and the free energies of formation of fayalite ($Fe_2SiO_4$) and magnetite ($Fe_3O_4$). Am Mineral 72:67

Padrón-Navarta JA, Hermann J, Garrido CJ, López Sánchez-Vizcaíno V, Gómez-Pugnaire MT (2010a) An experimental investigation of antigorite dehydration in natural silica-enriched serpentinite. Contrib Mineral Petrol 159:25–42. https://doi.org/10.1007/s00410-009-0414-5

Padrón-Navarta JA, Tommasi A, Garrido CJ, Sanchez-Vizcaino VL, Gomez-Pugnaire MT, Jabaloy A, Vauchez A (2010b) Fluid transfer into the wedge controlled by high-pressure hydrofracturing in the cold top-slab mantle. Earth Planet. Sci. Lett. 297:271–286. https://doi.org/10.1016/j.epsl.2010.06.029

Padrón-Navarta JA, Lopez Sanchez-Vizcaino V, Garrido CJ, Gomez-Pugnaire MT (2011) Metamorphic record of high-pressure dehydration of antigorite serpentinite to chlorite harzburgite in a subduction setting (Cerro del Almirez, Nevado-Filabride Complex, Southern Spain). J Petrol 52:2047–2078. https://doi.org/10.1093/petrology/egr039

Padrón-Navarta JA, López Sánchez-Vizcaíno V, Garrido CJ, Gómez-Pugnaire MT, Jabaloy A, Capitani GC, Mellini M (2008) Highly ordered antigorite from Cerro del Almirez HP-HT serpentinites SE Spain. Contrib Mineral Petrol 156(5):679–688

Padrón-Navarta JA, Sánchez-Vizcaíno VL, Hermann J, Connolly JAD, Garrido CJ, Gómez-Pugnaire MT, Marchesi C (2013)

Tschermak's substitution in antigorite and consequences for phase relations and water liberation in high-grade serpentinites. Lithos 178:186–196

Parkinson IJ, Arculus RJ (1999) The redox state of subduction zones: insights from arc-peridotites. Chem Geol 160:409–423. https://doi.org/10.1016/S0009-2541(99)00110-2

Philippot P, Selverstone J (1991) Trace-element-rich brines in eclogitic veins - implications for fluid composition and transport during subduction. Contrib Mineral Petrol 106(4):417–430. https://doi.org/10.1007/bf00321985

Piccoli F, Hermann J, Pettke T, Connolly JAD, Kempf ED, Duarte JFV (2019) Subducting serpentinites release reduced, not oxidized, aqueous fluids. Sci Rep 9:7. https://doi.org/10.1038/s41598-019-55944-8

Plank T, Langmuir CH (1998) The chemical composition of subducting sediment and its consequences for the crust and mantle. Chem Geol 145:325–394

Ranero CR, Morgan JP, McIntosh K, Reichert C (2003) Bending-related faulting and mantle serpentinization at the Middle America trench. Nature 425:367–373

Reynard B (2013) Serpentine in active subduction zones. Lithos 178:171–185

Scambelluri M, Pettke T, Rampone E, Godard M, Reusser E (2014) Petrology and trace element budgets of high-pressure peridotites indicate subduction dehydration of serpentinized mantle (Cima di Gagnone, Central Alps, Switzerland). Jour Petrol 55:459–498

Schmidt MW, Poli S (1998) Experimentally based water budgets for dehydrating slabs and consequences for arc magma generation. Earth Planet Sci Lett 163(1–4):361–379. https://doi.org/10.1016/s0012-821x(98)00142-3

Schmidt MW, Poli S (2014) Devolatization during subduction. In: Rudnick RL (ed) The crust. Treatise on geochemistry, 2nd edn. Elsevier, Amsterdam, pp 669–70

Schwartz S, Guillot S, Reynard B, Lafay R, Debret B, Nicollet C, Lanari P, Auzende AL (2013) Pressure–temperature estimates of the lizardite/antigorite transition in high pressure serpentinites. Lithos 178:197–210. https://doi.org/10.1016/j.lithos.2012.11.023

Song S, Su L, Niu Y, Lai Y, Zhang L (2009) $CH_4$ inclusions in orogenic harzburgite: evidence for reduced slab fluids and implication for redox melting in man-tle wedge. Geochim Cosmochim Acta 73:1737–1754

Stagno V, Frost DJ (2010) Carbon speciation in the asthenosphere: Experimental measurements of the redox conditions at which carbonate-bearing melts coexist with graphite or diamond in peridotite assemblages. Earth Planet Sci Lett 300:72–84. https://doi.org/10.1016/j.epsl.2010.09.038

Susaki J, Akaogi M, Akimoto S, Shimomura O (1985) Garnet-perovskite transition in CaGeO3: in situ X-ray measurements using synchrotron radiation. Geophys Res Lett 12:729–732

Tatsumi Y (1989) Migration of fluid phases and genesis of basalt magmas in subduction zones. J Geoph Res-Solid Earth and Planets 94(B4):4697–4707. https://doi.org/10.1029/JB094iB04p04697

**344**

Till CB, Grove TL, Withers AC (2012) The beginnings of hydrous mantle wedge melting. Contrib Mineral Petrol 163:669–688. https://doi.org/10.1007/s00410-011-0692-6

Trommsdorff V, Sánchez-Vizcaíno VL, Gómez-Pugnaire MT, Müntener O (1998) High pressure breakdown of antigorite to spinifex-textured olivine and orthopyroxene SE Spain. Contrib to Mineral Petrol 132:139–148. https://doi.org/10.1007/s004100050412

Truckenbrodt J, Ziegenbein D, Johannes W (1997) Redox conditions in piston-cylinder apparatus: The different behavior of boron nitride and unfired pyrophyllite assemblies. Am Miner 82(3–4):337-Tumiati S, Godard G, Martin S, Malaspina N, Poli S (2015) Ultra-oxidized rocks in subduction melanges? Decoupling between oxygen fugacity and oxygen availability in a Mn-rich metasomatic environment. Lithos 226:116–130. https://doi.org/10.1016/j.lithos.2014.12.008

Ulmer P, Trommsdorff V (1995) Serpentine stability to mantle depths and subduction-related magmatism. Science 268:858–861. https://doi.org/10.1126/science.268.5212.858

von Seckendorff V, O'Neill HStC, (1993) An experimental study of Fe-Mg partitioning between olivine and orthopyroxene at 1173, 1273 and 1423 K and 1.6 GPa. Contrib Mineral Petrol 113:196–207. https://doi.org/10.1007/BF00283228

Wunder B, Schreyer W (1997) Antigorite: High-pressure stability in the system MgO-SiO2-H2O (MSH). Lithos 41:213–227. https://doi.org/10.1016/S0024-4937(97)82013-0

Zhang J, Li B, Utsumi W, Liebermann R (1996) *In situ* X-ray observations of the coesite-stishovite transition: reversed phase boundary and kinetics. Phys Chem Miner 23:1–10. https://doi.org/10.1007/BF00202987